Flare Accelerated Electrons in Kappa-Distribution from X-Ray Spectra with Warm-Target Model

Yingjie Luo (骆英杰),[1] Eduard P. Kontar,[1] and Debesh Bhattacharjee[1]

[1]*School of Physics & Astronomy, University of Glasgow, G12 8QQ, Glasgow, UK*

ABSTRACT

X-ray observations provide essential and valuable insights into the acceleration and propagation of non-thermal electrons during solar flares. Improved X-ray spectral analysis requires a deeper understanding of the dynamics of energetic electrons. Previous studies have demonstrated that the dynamics of accelerated electrons of a few thermal speeds are more complex. To better describe the energetic electrons after injection, a model considering energy diffusion and thermalization effects in flare conditions (warm-target model) has recently been developed for Hard X-ray spectral analysis. This model has demonstrated how the low-energy cut-off, which can hardly be constrained in cold-target modeling, can be determined. However, the power-law form may not be the most suitable representation of injected electrons. The kappa distribution, which is proposed as a physical consequence of electron acceleration, has shown successful application in RHESSI spectral analysis. In this study, we employ the kappa-form injected electrons in the warm-target model to analyze two M-class flares, observed by RHESSI and STIX, respectively. The best-fit results show that the kappa-form energetic electron spectrum generates lower non-thermal energy when producing a similar photon spectrum in the fit range compared to the power-law form. We also demonstrated that the fit parameters associated with kappa-form electron spectrum can be well determined with small fit uncertainty. Further, the kappa distribution, which covers the entire electron energy range, enables the determination of key electron properties such as total electron number density and average energy in the flare site, providing valuable information on electron acceleration processes.

1. INTRODUCTION

Corresponding author: Yingjie Luo
Yingjie.Luo@glasgow.ac.uk

Solar flares are explosive energy-release events of which the emissions span over a wide electromagnetic wavelengths ranging from radio to γ-ray. In order to understand the acceleration mechanism and the transport of energetic electrons, it is crucial to know where and how the energy is released (Benz 2017). Energetic electrons from solar flares can be indirectly observed through X-ray and radio emissions. Due to the unique advantages, Hard X-ray (HXR) diagnostics is essential for determining the electron properties (see Holman et al. (2011); Kontar et al. (2011) for reviews). HXR emission observed from solar flares is dominantly due to electron-ion bremsstrahlung. The intensity of HXR emission is linearly proportional to the non-thermal electron density, so the observed HXR photon spectrum provides a straightforward relationship with the energetic electrons. Furthermore, HXR emission is less affected by propagation effects than radio emissions, resulting in minimal modification of the original electron properties during observations.

Over the past two decades, advanced X-ray instruments, such as the Reuven Ramaty High-Energy Solar Spectroscopic Imager (RHESSI; Lin et al. 2002) and the Spectrometer/ Telescope for Imaging X-rays (STIX; Krucker et al. 2020), have facilitated the collection of high-quality spectra and spectroscopic imaging. The frequently observed X-ray sources in the corona and chromosphere footpoints (Sui et al. 2002; Emslie et al. 2003; Battaglia & Benz 2006; Kontar et al. 2008; Shao & Huang 2009) strongly supports the 'thick-target' interpretation (Brown 1971; Syrovatskii & Shmeleva 1972), where flare-accelerated electrons propagate down to the dense chromosphere and deposit all their energy within the chromosphere. According to the thick target model, the observed X-ray photon spectrum is determined by the injected electron spectrum, bremsstrahlung cross-section, and the energy loss-rate within the target (Brown et al. 2003). When the energy of electrons is high compared to the target, i.e. $E \gg k_{\mathrm{B}}T$ (k_{B} is the Boltzmann constant, T is the temperature), the model is referred to as a cold target. In cold-target conditions, the kinetic energy loss is predominantly due to Coulomb collisions (Brown 1971; Lin & Hudson 1976), and while the other effects, such as return current Ohmic losses (Knight & Sturrock 1977; Emslie 1980; Zharkova & Gordovskyy 2006; Holman 2012; Alaoui & Holman 2017), could affect the results. While such a cold target model is widely utilized for the basis of HXR spectral analysis, observations necessitate that the coronal plasma during flares can reach high temperatures over 10^7 K, highlighting the need to improve the model. Studies have demonstrated that the behavior of electrons in the warm-target condition ($E \sim k_{\mathrm{B}}T$) is more complex and significantly different from what is predicted by the cold-target model. Emslie et al. (2003) highlighted a rapid drop in the energy loss rate in warm-target conditions, indicating a substantial overestimation of electron flux by the cold-target model in generating observed photon spectra. Additionally, collisional energy diffusion and thermalization (Galloway et al. 2005) have a significant impact on the dynamics of injected electrons. Furthermore, a physically self-consistent model requires consideration of both energy and spatial diffusions during electron transportation (Jeffrey et al. 2014). Taking into account these advances, Kontar et al. (2015, 2019) developed a warm-target model that provides a physically sound treatment of electron dynamics in the warm-target condition (referred to as the warm-target model in the following). This model includes collisional energy diffusion, suggesting that injected electrons thermalize within the target rather than losing all their energy and disappearing. The HXR spectrum generated by the warm-target model includes both the contributions from the the electrons in the cold-target chromosphere as well as the the component from the corona.

The warm-target model has been utilized to analyze RHESSI flares to more precisely fit the characteristics of non-thermal electrons (Kontar et al. 2019; Aschwanden et al. 2016, 2017). One significant chal-

lenge in inferring non-thermal electron properties is that the non-thermal emission is typically masked by the thermal emissions below 20-30 keV (Holman et al. 2011). This makes it difficult to determine the low-energy cut-off, E_c, which is essential in non-thermal electron energetics (see Aschwanden et al. 2019, for a review). This parameter, along with the closely-related non-thermal power are the key parameters to characterize the acceleration mechanism. The cold-target condition $E \gg k_{\mathrm{B}}T$ is typically applicable in the range over 20 keV, providing solely an upper limit for the low-energy cut-off E_c. On the other hand, the warm-target model considers the thermalization of injected electrons, which enables effectively constraining electron properties, as the spectra of thermalized electrons are proportional to the injected electrons. Kontar et al. (2019) have demonstrated that using the warm-target model with a power-law distribution can significantly enhance the accuracy of determining the low-energy cut-off E_c compared to the cold-target model.

However, it is important to recognize that the power-law form of the injected electron spectrum is not unique and not always the most suitable representation in many cases (Brown et al. 2006). The power-law distribution requires a low energy cut-off (E_c) to prevent infinite electron number. The presence of the low energy cut-off in the injected electron spectrum, while suggested to have physical significance in terms of the critical velocity of run-away and free acceleration (Holman & Benka 1992), results in a non-physical discontinuous electron distribution of Maxwellian plus the power law. Around the low-energy cut-off E_c, where positive distribution slope ($df/dv > 0$) exists, Langmuir waves are expected to generate and grow (Vedenov & Velikhov 1963; Drummond & Pines 1964; Emslie & Smith 1984; Hannah et al. 2009). The interaction between the waves will result in a flattened distribution around the low-energy cut-off (Krall & Trivelpiece 1973), suggesting the injected (accelerated) electron distribution should be nonincreasing function for all energies. On the other hand, the kappa distribution, consisting of a Maxwellian core and smoothly merged power-law tail, has been studied to represent accelerated electrons. The kappa distribution is often used to model the entire energetic electron spectrum from in-situ observations (Vandas 1989; Mace & Hellberg 1995; Collier et al. 1996; Maksimovic et al. 2005; Imada et al. 2011) and has emerged as a promising alternative for describing the accelerated electrons in HXR spectral fitting (Kašparová & Karlický 2009; Oka et al. 2013, 2015; Battaglia et al. 2015; Effenberger et al. 2017). Previous studies have shown that while spatially integrated spectra cannot be well-fitted only with the electrons obeying a kappa distribution, kappa-form accelerated electrons with a prominent thermal component yields promising results.

In addition to not requiring an arbitrary energy cut-off E_c, the adoption of a kappa-form injection offers several advantages over the power-law distribution. First, the kappa-form electron spectrum is believed to result from acceleration out of thermal equilibrium, and its parameters can provide crucial information on electron acceleration. Various studies have delved into the origin of the kappa distribution from different perspectives, including collisional relaxation along with wave-particle interaction (Ma & Summers 1998; Vocks & Mann 2003), beam-plasma interactions (Yoon et al. 2006; Ryu et al. 2007; Rhee et al. 2006). Moreover, originating from the Fokker-Planck equation, Bian et al. 2014 has pointed out that the kappa electron distribution results from stochastic acceleration in the presence of Coulomb collisions and velocity diffusion, specifying insight into electron kinetics during solar flares. Similarly, simulations of electron acceleration during magnetic reconnection lead to a distribution resembling a kappa-distribution (Arnold et al. 2021). Another advantage of the electron spectrum in kappa distribution over the power-law distribution is its entire electron kinetic energy coverage. Kappa distribution can provide electron information at low energy ($\sim$keV), which is not sensitive to X-ray instruments

but can be observed through other diagnostics such as EUV observations. This allows for a more comprehensive study of electron distribution through multi-wavelength observations, providing additional constraints (Oka et al. 2015; Battaglia et al. 2015). Furthermore, due to its whole electron energy coverage and convergent nature, the kappa distribution allows for the determination of parameters such as electron number density and average electron energy, which is not achievable with the power-law distribution. The kappa distribution is closely related to the thermal properties of the ambient plasma. Parameters such as electron number density and average electron energy can be directly compared with the corresponding thermal properties of the pre-accelerated plasma, serving as an important constraint and cross-check.

The paper investigates the spectrum of accelerated (injected) electrons in solar flares. Section 2 discusses relationship between kappa-form injected electron spectrum and the mean electron flux based on the warm-target model. We utilize the warm-target model with kappa form injected electrons to analyze solar flares observed by RHESSI on February 24, 2011, and by STIX on March 28, 2022. The best-fit results and a comparison between the kappa and power-law form injection is provided in Section 3. Section 4 discusses the uncertainty of fitting parameters related to the kappa distribution with different approaches. The resulting characteristics such as electron number density and average electron energy are also shown. The findings and the physical significance of the derived kappa parameters are summarized and discussed in Section 5.

2. SOURCE-INTEGRATED SPECTRUM FROM KAPPA-FORM INJECTED ELECTRONS

Brown et al. (2003) highlighted the concept of the source-integrated density-weighted mean electron flux $\langle nVF \rangle(E)$ [electrons cm^{-2}s^{-1}keV^{-1}] and expressed the observed HXR spectrum $I(\varepsilon)$ [photons cm^{-2}s^{-1}keV^{-1}] as:

$$I(\varepsilon) = \frac{1}{4\pi R^2} \int_\varepsilon^\infty Q(\varepsilon, E)\langle nVF \rangle(E)\,dE, \tag{1}$$

where R is the distance between the observer and the Sun, and $Q(\varepsilon, E)$ is angle-averaged bremsstrahlung cross-section (see discussion in Kontar et al. (2011) for RHESSI). Determination of the mean electron flux from the observed photon spectrum requires only the well-studied bremsstrahlung cross-section (Haug 1998). To obtain the injected electron rate spectrum $\dot{N}(E)$ [electrons s^{-1}keV^{-1}] from the obtained mean electron flux, a model for the dynamics of injected electrons is necessary. The commonly used cold-target model establishes the relationship between mean electron flux and injected electron rate as

$$\langle nVF \rangle(E) = \frac{E}{K} \int_E^\infty \dot{N}(E_0)\,dE_0\,, \tag{2}$$

were $K = 2\pi e^4 \ln(\Lambda)$ is collision parameter, e [esu] is the elementary charge and $ln(\Lambda)$ is the Coulomb logarithm (Spitzer 1962). To account for the electron dynamics in the warm-target corona and cold chromosphere, Kontar et al. (2015) included the energy diffusion, transport and thermalization of the accelerated electrons, rewriting Equation (2)

$$\langle nVF \rangle(E) = \frac{1}{2K}E\,e^{-E/k_{\mathrm{B}}T} \int_{E_{min}}^E \frac{e^{E'/k_{\mathrm{B}}T}}{E'G(\sqrt{E'/k_{\mathrm{B}}T})}\,dE' \times \int_{E'}^\infty \dot{N}(E_0)\,dE_0\,. \tag{3}$$

Kontar et al. (2019) further simplify equation (3) and re-write as:

$$\langle nVF\rangle(E) \approx \Delta EM\sqrt{\frac{8}{\pi m_e}}\frac{E}{(k_{\rm B}T)^{3/2}}e^{-E/k_{\rm B}T} + \frac{E}{K}\int_E^\infty \dot{N}(E_0)\,dE_0\,, \tag{4}$$

where ΔEM, referred as 'thermalized emission measure', is due to the thermalization of accelerated electrons, can be explicitly written as

$$\Delta EM \approx \frac{\pi}{K}\sqrt{\frac{m_e}{8}}(k_{\rm B}T)^2\frac{\dot{N}_0}{E_{\rm min}^{1/2}}\,, \quad \text{where} \quad E_{\rm min} \approx 3k_{\rm B}T(\frac{5\lambda}{L})^4\,, \tag{5}$$

and $\dot{N}_0$ [electrons s^{-1}] $= \int_0^\infty \dot{N}(E)\,dE$ is the total electron injection (acceleration) rate, $\lambda = (k_{\rm B}T)^2/2Kn$ is the collisional mean free path. The half loop length L, number density n, and temperature T are the parameters associated with the coronal part of the loop. Equation 4 consists of two parts, refer as the thermalized and non-thermal components, corresponding to the warm- (coronal) and cold-target conditions, respectively. It is worth noting that the thermalized component is proportional to the total injected electron rate $\dot{N}_0$, which is why this model is effective in constraining the nonthermal component when fitting the observed X-ray spectrum. This warm-target model 'f_thick_warm', which utilizes Equations 4 and 5, is implemented in Solar Software (SSW) and OSPEX package (Schwartz et al. 2002; Tolbert & Schwartz 2020). Function 'f_thick_warm' utilizes the commonly employed broken power-law form of injected electrons, and it is worth noting that the warm-target model (Equations 4 and 5) can accept any electron injection rate form. As mentioned earlier, the use of a kappa distribution for injection is a promising alternative and has been applied to fit the RHESSI spectra.

Bian et al. 2014 derives the kappa distribution as a result of stochastic acceleration in collisional plasma:

$$f_k(v) = \frac{n_k}{\pi^{3/2}v_{\rm te}^3\kappa^{3/2}}\frac{\Gamma(\kappa)}{\Gamma(\kappa - 3/2)}(1 + \frac{v^2}{\kappa v_{\rm te}^2})^{-\kappa}\,, \tag{6}$$

where $v_{\rm te}$ is the thermal speed $(1/2m_e v_{\rm te}^2 = k_{\rm B}T_\kappa)$, and κ is the kappa index, which importantly represents the ratio between the acceleration $\tau_{\rm acc}(v)$ and collisional deceleration $\tau_c(v)$ time scales $\kappa = \frac{\tau_{\rm acc}(v)}{2\tau_c(v)}$. While different formats of the kappa distribution exist (see, e.g. Kašparová & Karlický 2009; Oka et al. 2013), they are identical in essence and only differ in their format and use of parameters. Furthermore, the physical interpretation of κ vary when additional factors are are taken into account. In this study, we have chosen to adopt Equation 6 for the kappa distribution.

The relationship between injected electron rate spectrum and electron distribution for velocity is $\dot{N}(E)dE = Av f_k(v)d^3v$, A is the injection area. For isotropic electron distribution $(d^3v = 4\pi v^2 dv)$, the injected electron rate spectrum becomes (see red curves in Figure 1):

$$\dot{N}(E) = A\frac{n_k\Gamma(\kappa)}{\Gamma(\kappa - 3/2)\kappa^{3/2}}\sqrt{\frac{8}{\pi m_e k_{\rm B}T_\kappa}}\frac{E/k_{\rm B}T_\kappa}{(1 + E/\kappa k_{\rm B}T_\kappa)^\kappa}\,, \tag{7}$$

where n_k [cm^{-3}] $= \int f_k(v)\,d^3v$ is the total electron number density, $\Gamma(x)$ is the gamma function. The total injection rate becomes:

$$\dot{N}_0 = \int_0^\infty \dot{N}(E)\,dE = 2An_k\sqrt{\frac{2k_{\rm B}T_\kappa}{m_e}}\frac{\kappa^{1/2}}{(\kappa - 2)B(\kappa - 3/2, 1/2)}\,, \tag{8}$$
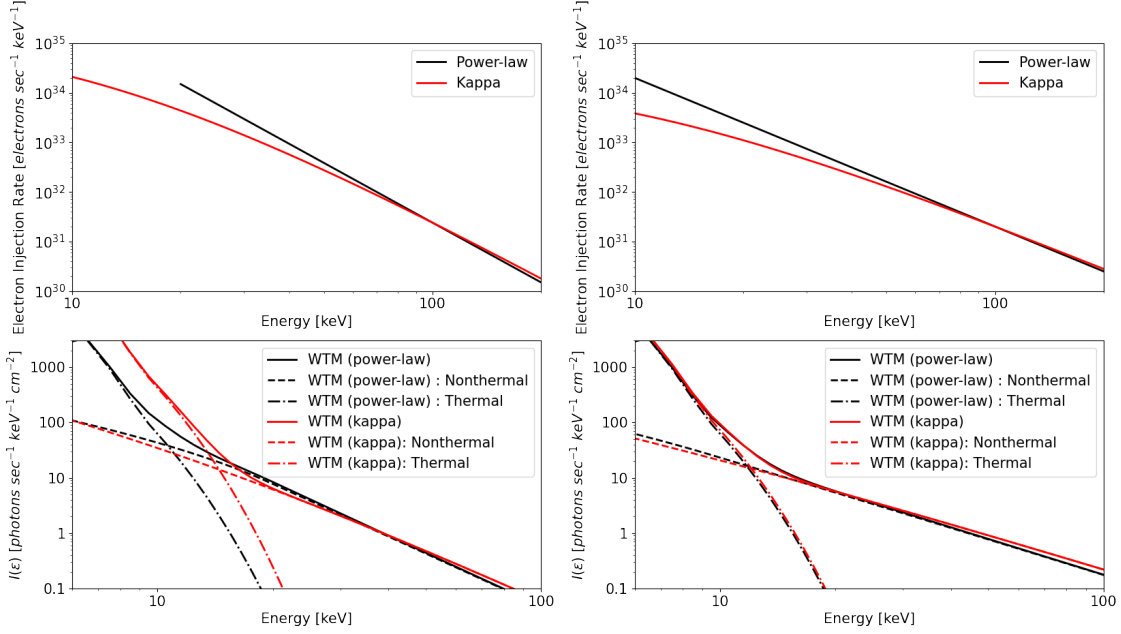
Figure 1. Top Panels: The electron injection rate spectrum from power-law form and kappa form distributions. For case shown in the left, power-law form injection has a parameter of $\dot{N}_0 = 1 \times 10^{10}$ electrons s^{-1}, $E_c = 20$ keV, and $\delta = 4$, and the kappa-form injection is set to $\dot{N}_0 = 6.8 \times 10^{10}$ electrons s^{-1}, $k_B T_\kappa = 1.5$ keV, and $\kappa = \delta + 1 = 5$. The selection is for satisfying $\dot{N}_\kappa(E_1) = \dot{N}_{Max}(E_1)$, when $E_1 = 100$ keV. Case shown in the right panel are with the power-law parameters: $\dot{N}_0 = 1 \times 10^{10}$ electrons s^{-1}, $E_c = 10$ keV, $\delta = 3$, condition of a high proportion of nonthermal electrons. Same certification are used to obtain the kappa-form electron spectrum: $\dot{N}_0 = 1.17 \times 10^{10}$ electrons s^{-1}, $k_B T_\kappa = 1.5$ keV, and $\kappa = 4$. Bottom Panel: The photon spectrum, based on the warm-target model (WTM), generated by the electron injection in the top panel with a coronal condition of $L_{\text{loop}} = 30$ Mm, $n_{\text{loop}} = 5 \times 10^{10}$ cm^{-3}, and $k_B T_{\text{loop}} = 1.5$ keV. Photon spectrum from power-law and kappa-form injection are plotted in black and red, respectively. Solid curves represent the total photon spectrum, while the dashed and dot-dashed curves represent the 'nonthermal' and 'thermalized' components, respectively.

where $B(x, y)$ is the beta function. Equation 7 can be expressed as:

$$\dot{N}(E) = \frac{\dot{N}_0}{k_B T_\kappa} \frac{(\kappa - 1)(\kappa - 2)}{\kappa^2} \frac{E/k_B T_\kappa}{(1 + E/\kappa k_B T_\kappa)^\kappa}. \tag{9}$$

According to Equation 4, the mean electron flux from a kappa-form injected electrons is given by (Equation 17, Appendix of Kontar et al. 2019):

$$\langle nVF \rangle(E) \approx \Delta EM \sqrt{\frac{8}{\pi m_e}} \frac{E}{(k_B T)^{3/2}} e^{-E/k_B T} + \dot{N}_0 \frac{E}{K} \frac{1 + (1 - 1/\kappa)E/k_B T_\kappa}{(1 + E/\kappa k_B T \kappa)^{\kappa - 1}}. \tag{10}$$

For high energy electrons, the kappa distribution can be well approximated by a power-law distribution with a spectral index $\kappa - 1$. Figure 1 shows that the two distributions have an identical injection rate near 100 keV. However, in the energetically important deka-keV range, kappa distribution is distinct from a power-law distribution, and thus, a different photon spectrum emerges. Figure 1 illustrates the electron injection rate (top panels, red and black for kappa- and power-law injection ,respectively)

and the resulting photon spectra (bottom panels) generated by the warm-target model in a typical flare coronal condition ($L_{\mathrm{loop}} = 30\,\mathrm{Mm}$, $n_{\mathrm{loop}} = 5 \times 10^{10}\,\mathrm{cm}^{-3}$, and $k_{\mathrm{B}}T_{\mathrm{loop}} = 1.5\,\mathrm{keV}$).

3. APPLICATION OF THE WARM-TARGET MODEL TO OBSERVATIONS

In this section, we apply the warm-target model to analyze two well-observed flare event. One on 2011 February 24, observed by the RHESSI and one on 2022 March 28 observed by the STIX, both events are situated in the limb and providing spectroscopic images with two footpoint and looptop sources. The warm-target model with kappa-form electron injection (function *f_thick_warm_kappa*, based on Equation 10) encompasses parameters of kappa distribution (total electron injection rate $\dot{N}_0$, kappa temperature T_κ, and kappa index κ) and thermal properties of the target coronal loop (the half loop length L, number density n_{loop}, and temperature T_{loop}).

In this study, the thermal properties of the target plasma are determined by the HXR observations of the thermal component. Following the approach outlined in Kontar et al. (2019), the thermal component of the X-ray spectra prior to the HXR burst can provide the plasma temperature (T) and emission measure (EM). Moreover, the HXR spectroscopic imaging can estimate the coronal loop length (L) and coronal X-ray loop source size for determining the electron number density (n_{th}). While this method is straightforward, we recognize that other methods, such as differential emission measure analysis (DEM; see algorithms from Craig & Brown 1976; Hannah & Kontar 2012; Cheung et al. 2015) from EUV flare context or combining X-ray data with EUV data (Inglis & Christe 2014; Battaglia et al. 2015), can yield thermal properties (Battaglia & Kontar 2013; Battaglia et al. 2015).

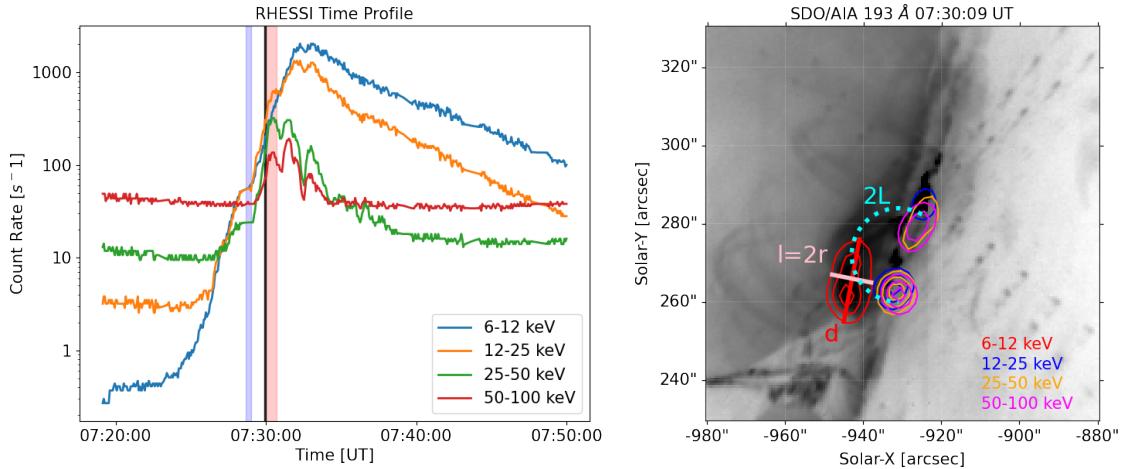### 3.1. *2011 February 24 RHESSI flare*

Figure 2. Left panel: RHESSI light curves detailing a GOES-class M3.5 solar flare on February 24th, 2011. The blue, black, and red shadowed regions denote the chosen time frames for background, pre-burst, and HXR burst, respectively, for the subsequent spectral fit. Right Panel: RHESSI contours (50, 70, 90% of the maximum, time range used for imaging is the red shadowed region in the left panel) overlaied on the SDO/AIA 193 Å flare context (invert gray color scale). A cyan-colored semi-circular loop (half loop length L) that traverses through two footpoints and the looptop source is plotted. The 50% contour of the loop top source also provide the characteristic lengths ($l = 2r$ and d) necessary for calculating the loop top source size.

The first flare of study is a GOES-class M3.5 flare located on the eastern limb from the Earth's perspective. The flare occurred on February 24, 2011 with GOES Soft X-ray flux peaked at ∼07:35 UT (see
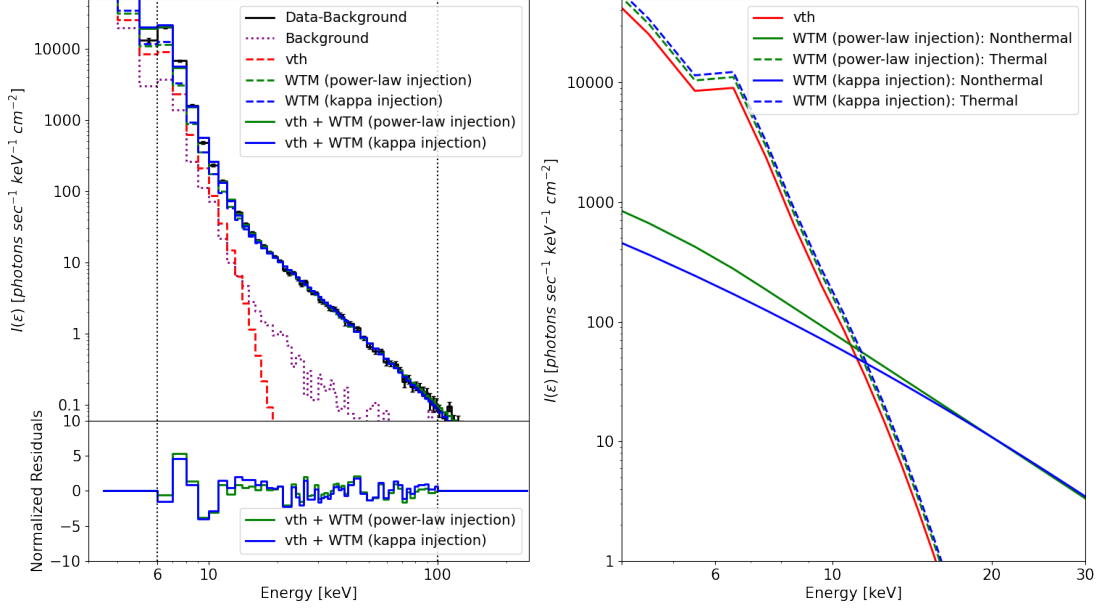
Figure 3. Left panel: Fit photon spectrum of the 2011 February 24 flare. The fit was done twice, using functions *f_vth* (iso-thermal, red dashed curve) and *f_thick_warm/f_thick_warm_kappa* (warm-target model with power-law and kappa form electron injection, green and blue dashed curve, respectively). The observed background subtracted spectrum is shown in black (time of burst and background is shown as red and blue shadowed regions in Figure 2 left panel), and the fit range spans from 6 to 100 keV. Normalized residuals, which are the difference between observed (black curve) and fit (green and blue solid curves for different fit) photons divided by error, are also displayed in the bottom. Right panel: the photon spectrum of the iso-thermal (red) and warm-target model (power-law and kappa form injection is in green and blue, respectively). The nonthermal and thermal components (see Equation 4) of the warm-target model are presented in solid and dashed curves, respectively.

Battaglia & Kontar 2011, 2012; Stackhouse & Kontar 2018, for previous studies of this event). Our attention is drawn to the first HXR peak at approximately 07:30 UT (red shadowed time range in Figure 2 left panel). The HXR spectroscopic imaging of the burst displays a 'classical' configuration of the loop top source and two HXR footpoints (Figure 2 right panel). The X-ray observations from the RHESSI of the selected HXR burst benefits from the low/negligible pile-up effect. Furthermore, RHESSI was in optimal working condition during the flare, providing more functional detectors.

For spectral analysis, we first gather the thermal properties of the target coronal loops according to the images of the burst (07:30:00 to 07:30:44 UT, Figure 2 left panel red shadowed time range) and spectra before the interval analysed (short time interval closely prior to the burst analysed, refer as 'pre-burst' in the following, in this case 07:29:52 to 07:30:00 UT, Figure 2 left panel black shadowed time range). In the analysis of the pre-burst X-ray spectra, we utilize functions *f_vth* (iso-thermal) and *f_thick2* (cold-thick-target). In this stage, we focus solely on the thermal plasma parameters and can overlook the constraints associated with using the cold-target model. *f_vth* from the best-fit result of the pre-burst spectra provides us with the plasma temperature ($k_B T_0 = 1.30 \, \text{keV}$) and emission measure ($EM_0 = 0.127 \times 10^{49} \, \text{cm}^{-3}$) before the injection/acceleration of nonthermal electrons. Additionally, we use X-ray spectroscopic imaging (Figure 2 right panel) to estimate the size of the X-ray source and target coronal loop. We determine the source size in various dimensions (see pink and red solid lines in
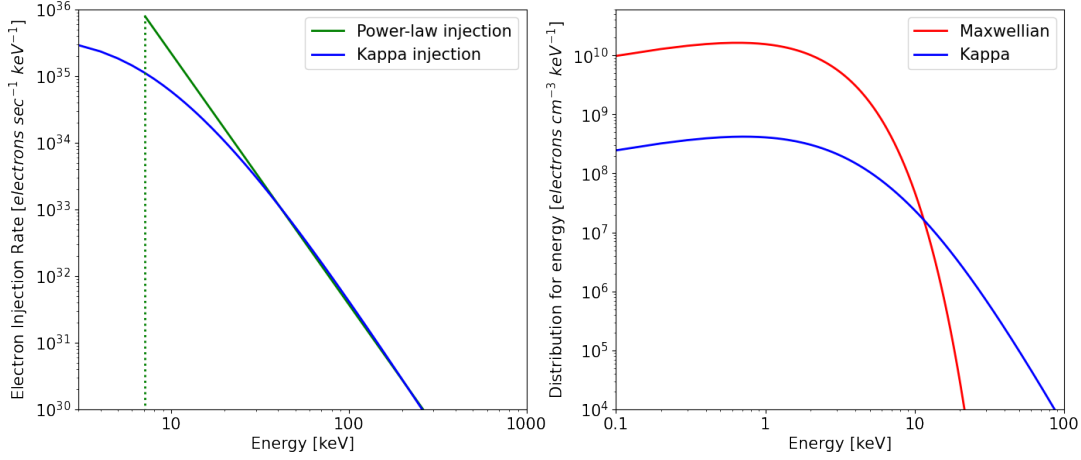
Figure 4. Left panel: The injected electron rate spectrum $\dot{N}(E)$ inferred from the warm-target fit results (see Table 1 for fitted parameters). The green and blue curves correspond to the power-law ($E_c = 7.13\,\text{keV}$) and kappa form electron injection, respectively. Right panel: the distribution of electrons for the energy $f_k(E)$ ($f_k(E)dE = f_k(v)d^3v$) of the fitted kappa distribution (blue curve, total electron number density $n_k = 1.67 \times 10^9\,\text{cm}^{-3}$, from Equation 8) and pre-burst thermal Maxwellian distribution (red curve, total electron number density $n_k = n_{th} = 4.4 \times 10^{10}\,\text{cm}^{-3}$).

Parameters	vth+WTM(power-law)	vth+WTM(kappa)	
EM [$10^{49}\,\text{cm}^{-3}$]	0.127	0.127	Fixed
$k_B T$ [keV]	1.30	1.30	Fixed
n_{loop} [$10^{10}\,\text{cm}^{-3}$]	4.4	4.4	Fixed
$k_B T_{\text{loop}}$ [keV]	1.30	1.30	Fixed
L [Mm]	15.8	15.8	Fixed
$\dot{N}_0$ [10^{35} electrons sec^{-1}]	20.3 ± 0.8	22.5 ± 0.8	Free
δ	3.77 ± 0.02	N/A	Free
κ	N/A	5.14 ± 0.04	Free
E_c [keV]	7.13 ± 0.19	N/A	Free
$k_B T_\kappa$ [keV]	N/A	1.29 ± 0.04	Free
χ^2	1.93	2.11	N/A
Power [10^{28} erg/s]	3.62	2.23 for total; 1.41 above E_c	N/A

Table 1. The parameters and fit results of 2011 February 24 M3.5 flare using the warm-target model. The iso-thermal component and thermal properties of the warm-target model are fixed, and properties associated with the accelerated electron spectrum are set free. The reduced χ^2 and nonthermal electron power (P) are also listed. For the convenience of comparison, the nonthermal power produced by the kappa-form electron spectrum above power-law low energy cutoff E_c is also shown.

Figure 2 right panel, $r = l/2 = 3.7\,\text{Mm}$ and $d = 15.3\,\text{Mm}$, respectively) by considering the 50% contour of X-ray loop top sources. The cross-area can be calculated as $A = \pi r^2 = 4.21 \times 10^{10}\,\text{cm}^2$, and the source volume can be obtained through the cylindrical formula: $V = A \times d = \pi r^2 d = 6.46 \times 10^{26}\,\text{cm}^3$. Thus the thermal electron number density can be estimated using $n_{\text{loop}} = \sqrt{EM_0/V} = 4.4 \times 10^{10}\,\text{cm}^{-3}$. To obtain the coronal loop length, we construct a semi-circular loop (see cyan dashed line in Figure 2

right panel) that connects two footpoints and passes through the loop top source. Consequently, we determine the thermal properties: loop temperature ($k_B T_{\text{loop}} = k_B T_0 = 1.30\,\text{keV}$), loop number density ($n_{\text{loop}} = \sqrt{EM_0/V} = 4.4 \times 10^{10}\,\text{cm}^{-3}$), and the the half-loop length ($L = 15.8\,\text{Mm}$).

Once the thermal properties are determined, we proceed to fit the spectra of the burst time interval (07:30:00 to 07:30:44 UT) in 6–100 keV using functions *f_vth* and *f_thick_warm_kappa*. In function *f_vth*, the temperature and emission measure are fixed according to the pre-burst spectra ($T = T_0$, $EM = EM_0$). The warm-target algorithm propose that the emission measure during the burst interval is a combination of the emission measure from the pre-burst and the emission measure of thermalized injected electrons ($EM = EM_0 + \Delta EM$, photon spectrum associated with EM_0 and ΔEM are plotted as the red solid curve and dashed curves in Figure 3 right panel). Since the plasma is slowly changing during the 40 sec interval (electron diffusion time along the loop ~56 seconds, use Kontar et al. (2019) Equation 11), the parameters in *f_thick_warm_kappa* related to thermal properties of the loop are fixed in the fit (the half loop length L, number density n_{loop}, temperature T_{loop}, and the relative elemental abundances, default to be 1 (Landi et al. 2013)). The parameters of kappa-form injection spectrum (total electron injection rate $\dot{N}_0$, kappa temperature T_κ, and kappa index κ, except the high energy cut_off E_{high} fix to 10^4 keV) are determined from the fit. Moreover, fit with a single power-law electron injection in the warm-target model '*f_thick_warm*' was performed for comparison: the total injection rate $\dot{N}_0$, power-law index δ, and low-energy cut_off E_c are free, the break-energy E_{break} and high energy cut_off E_{high} is fixed to 10^4 keV. The best-fit parameters (see Table 1) and generated photon spectra are plotted in Figure 3 (blue and green curves for warm-target model with kappa and power-law form injection, respectively, same color representation for the normalized residuals in the bottom panel).

The fit using the warm-target model, with kappa and power-law forms of electron injection, both produces favorable fit results with reasonable parameters. With the systematic uncertainty of 0.02, which is default for RHESSI in OSPEX, the reduced χ^2 is 1.93 and 2.11 for the fit with kappa and power-law forms of electron injection, respectively. From Figure 3 left bottom panel, the significant normalized residuals remain below 12 keV, where thermal bremsstrahlung dominates. This may arise from the use of the iso-thermal assumption *f_vth* for the thermal emission (Jeffrey et al. 2015). From the photon spectrum made by individual component (Figure 3 right panel), we found that for this HXR burst, the emission measure contributed by the thermalized injected electron (ΔEM, dashed curves) is of comparable magnitude to the iso-thermal component (EM, red solid curve). Here, we note that although the ratio of $\Delta EM/EM$ is affected by the pre-burst timing chosen, all reasonable selections of pre-burst timing can yield acceptable fit results. The different ratios only arise from the identification of pre-accelerated plasma.

In Figure 4 left panel, we plot the injected electron rate spectrum (blue and green curves represent the best-fit kappa and power-law form injection, respectively). We noticed that the power-law and kappa forms electron injection exhibit similarly between 40-100 keV but behave differently approximately below 30 keV. At the power-law low energy cut-off E_c, the electron injection rate $\dot{N}(E_c)$ of the kappa distribution is almost one order of magnitude smaller (1.11 vs. 7.88 $\times 10^{35}$ electrons $\text{sec}^{-1}\,\text{keV}^{-1}$ for kappa and power-law form injection, respectively). Additionally, the fitted injected electron spectrum in the kappa distribution decreases more rapidly ($\kappa > \delta + 1$) at higher energy. Although the best-fit electron spectrum in kappa and power-law form have a similar total injection rate ($\dot{N}_0 = 22.5$ vs. 20.3 $\times 10^{35}$ electrons sec^{-1} for kappa and power-law form injection, respectively), the power-law electron spectrum produces a more substantial nonthermal power than the kappa form electron spectrum (see

Table 1, 3.62 vs 2.23 $\times 10^{28}$ erg/s, $\frac{P_\kappa}{P_{power-law}} \approx 0.61$). Moreover, for kappa form electron spectrum, the nonthermal power produced by the electrons above power-law low energy cut_off E_c is 1.41 $\times 10^{28}$ erg/s. The equations used for calculating the power are listed below, for power-law distribution:

$$P = \int_{E_c}^{\infty} E'N(E')\,dE' = \frac{\delta - 1}{\delta - 2}E_C\dot{N}_0. \tag{11}$$

For kappa distribution:

$$P = \int_{E_1}^{E_2} E'N(E')\,dE' = \frac{\dot{N}_0}{(k_\mathrm{B}T_\kappa\kappa)^2(\kappa - 3)}(k_\mathrm{B}T_\kappa\kappa + E'')\times$$
$$(\frac{E''}{k_\mathrm{B}T_\kappa\kappa} + 1)^{-\kappa}[2(k_\mathrm{B}T_\kappa\kappa)^2 + 2k_\mathrm{B}T_\kappa(\kappa - 1)\kappa E'' + (\kappa^2 - 3\kappa + 2)E''^2]\Big|_{E_1}^{E_2}. \tag{12}$$

Thus

$$P = \int_0^{\infty} E'N(E')\,dE' = \frac{2\dot{N}_0 k_\mathrm{B}T_\kappa\kappa}{\kappa - 3}; \tag{13}$$

$$P = \int_{E_c}^{\infty} E'N(E')\,dE' = \frac{\dot{N}_0}{(k_\mathrm{B}T_\kappa\kappa)^2(\kappa - 3)}(k_\mathrm{B}T_\kappa\kappa + E_c)\times$$
$$(\frac{E_c}{k_\mathrm{B}T_\kappa\kappa} + 1)^{-\kappa}[2(k_\mathrm{B}T_\kappa\kappa)^2 + 2k_\mathrm{B}T_\kappa(\kappa - 1)\kappa E_c + (\kappa^2 - 3\kappa + 2)E_c^2]. \tag{14}$$

We also include a distribution plot ($f_k(E)$, $f_k(E)dE = \langle f_k(v)\rangle d^3v$) of the accelerated kappa-form electrons (blue curve in Figure 4 right panel, $n_k = 1.67 \times 10^9$ cm^{-3}, calculated from Equation 8, here $A = 4.21 \times 10^{10}$ cm^2). The Maxwellian thermal distribution, which is take from the iso-thermal component f_vth (total electron number density $n_k = n_{th} = 4.4 \times 10^{10}$ cm^{-3}, $k_\mathrm{B}T = 1.30$ keV), is also shown in red curve for comparison. We will provide a more detailed discussion of the parameters obtained in the following section.

3.2. *2022 March 28 STIX flare*

We conducted the same spectral analysis to the other well-observed GOES class M4.0 flare on March 28, 2022. GOES Soft X-ray flux peaks at $\sim$ 11:29 UT; the flare-associated HXR bursts were detected by STIX onboard the Solar Orbiter (Sol-O; Müller et al. 2020). The STIX temporal profile is shown in Figure 5 left panel, with the time difference of 335.7 seconds between the Sol-O and the Earth has been applied to the STIX data. The flare site is situated in the eastern limb from Sol-O's perspective. Extreme Ultraviolet Imager (EUI; Rochus et al. 2020)/Full Sun Imager (FSI) provides EUV context from the same viewpoint (Figure 5 right panel). This flare comprises several HXR bursts, and our focus is on the burst occurring at approximately 11:21 UT (red shadowed time range in Figure 5 left panel).

The selected burst and pre-burst time ranges for this flare are 11:21:24–11:21:44 UT and 11:21:12–11:21:17 UT (Figure 5 left panel red and black shadowed regions), respectively. For this particular
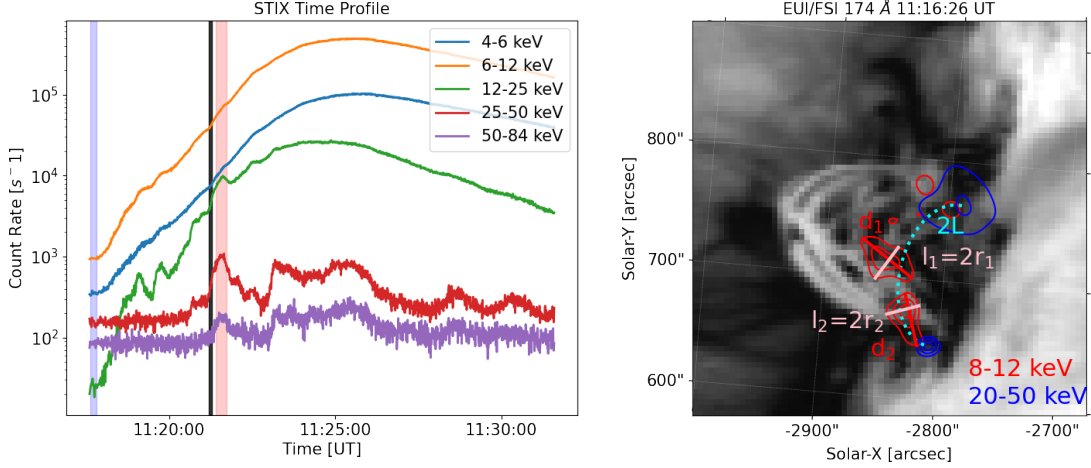
Figure 5. Left panel: STIX light curves (time has been shifted to the estimated timing observed on earth) detailing a GOES-class M4.0 solar flare peaking at ~11:29 UT on March 28th, 2022. The blue, black, and red shadowed regions denote the chosen time frames for background, pre-burst, and HXR burst of study, respectively, for the subsequent spectral fit. Right Panel: STIX contours (50, 70, 90% of the maximum, time range used for imaging is the red shadowed region in the left panel) overlaid on the EUI/FSI 174 Å flare context (invert gray color scale, use image at 11:16 UT instead of 11:26 UT to avoid the over-exposure of the flare site). A cyan-colored semi-elliptical loop (half loop length L) that traverses through two footpoints and the looptop source is plotted. The 50% contour of the two loop top sources provide the characteristic lengths ($l = 2r$ and d, northern and southern loop top sources marked with '1' and '2', respectively) necessary for calculating the loop top source size.

event, bottom pixels have a noticeable larger counts than the top pixels. Thus, spectrum for fitting and spectroscopic imaging relies solely on the data from the bottom pixels. The fit range is set to be 6 – 50 keV. The pre-burst spectra yield emission measure and temperature values of $k_B T_0 = 1.67$ keV and $EM_0 = 0.0532 \times 10^{49}$ cm^{-3}. Figure 5 right panel displays X-ray spectroscopic images using the CLEAN algorithm (Högbom 1974) and are overlaid on EUI/FUI 174 Å flare context. Two looptop sources (red contours, 8-12 keV), of which the southern one existed before the flare (See Figure 2 in Purkhart et al. 2023, for detailed flare evolution), and two footpoint sources (blue contours, 20-50 keV) are observed. According to the 50% contour of the two loop top sources, we obtain the source size in different dimensions ($r_1 = l_1/2 = 3.4$ Mm, $r_2 = l_2/2 = 3.2$ Mm, pink lines, and $d_1 = 12.1$ Mm, $d_1 = 9.6$ Mm, red lines). The cross-area (using northern source, $A = \pi r_1^2 = 3.64 \times 10^{10}$ cm^2) and source volume ($V = \pi r_1^2 d_1 + \pi r_2^2 d_2 = 7.59 \times 10^{26}$ cm^3) can be calculated accordingly. The constructed semi-elliptical coronal loop (cyan dashed line in Figure 5 right panel), which rooted at two HXR footpoint sources and passing through the loop top sources, features a half-loop length of $L = 18.4$ Mm. As a result, we can determine the target loop's thermal properties ($k_B T_{\rm loop} = k_B T_0 = 1.67$ keV and $n_{\rm loop} = \sqrt{EM_0/V} = 2.4 \times 10^{10}$ cm^{-3}).

The best-fit results using *f_vth* and *f_thick_warm_kappa/f_thick_warm* are shown in Figure 6 and Table 2. To account for STIX calibration uncertainty, which is still unknown, 6% systematic error was added in OSPEX following Jeffrey et al. (2024). From the Figure 7 left panel, distinct difference between the kappa and power-law form injection electron spectrum was noted below 30 keV, consistent with the findings from the 2011 February 24 flare. For this event, low energy cut_off E_c obtained from *f_thick_warm* is 12.46 keV. For comparison, the injection rate $\dot{N}(E = E_c)$ is 0.641 vs. 4.21 $\times 10^{35}$ electrons sec^{-1} keV^{-1} for kappa and power-law form injection, respectively. The kappa form elec-
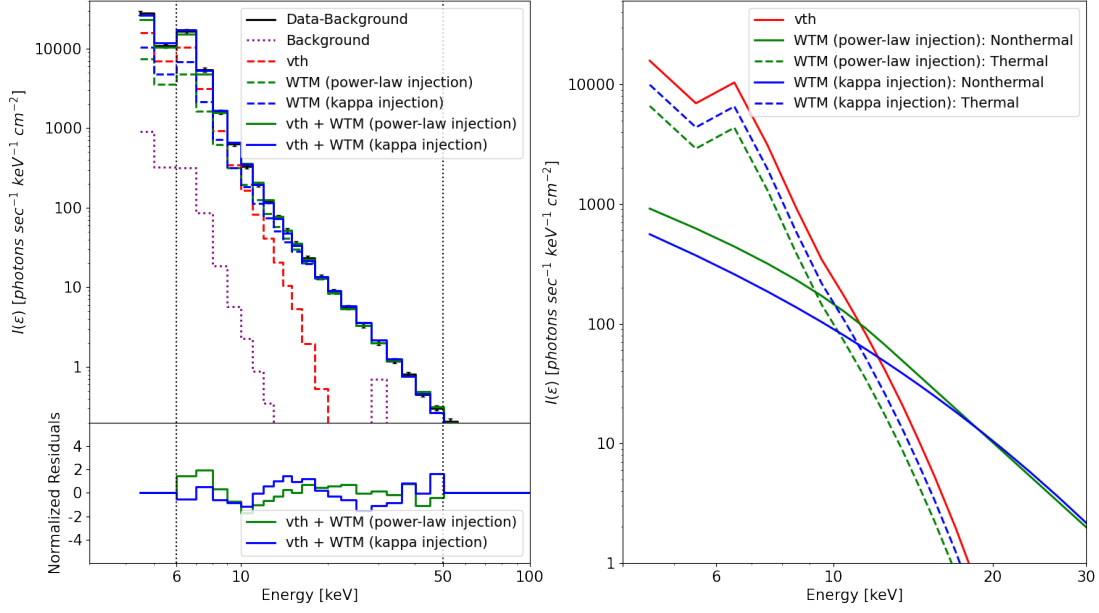
Figure 6. Left panel: Fit photon spectrum of the 2022 March 28 M4.0 flare. Same as Figure 3, the fit was done twice, using functions *f_vth* (iso-thermal, red dashed curve) and *f_thick_warm*/*f_thick_warm_kappa* (warm-target model with power-law and kappa form electron injection, green and blue dashed curve, respectively). The observed background subtracted spectrum is shown in black (time of burst and background is shown as red and blue shadowed regions in Figure 5 left panel), and the fit range spans from 6 to 50 keV. Normalized residuals are displayed in the bottom. Right panel: the photon spectrum of the iso-thermal (red) and warm-target model (power-law and kappa injection, in green and blue, respectively). The nonthermal and thermal components of the warm-target model are presented in solid and dashed curves, respectively.
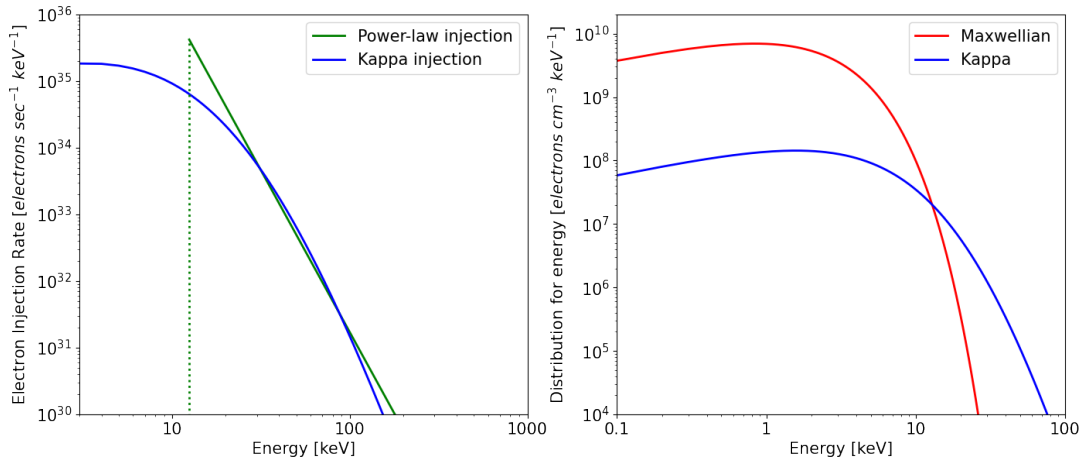
Figure 7. Left panel: The injected electron rate spectrum $\dot{N}(E)$ inferred from warm-target fit results (see Table 2 for fitted parameters). The green and blue curves correspond to the power-law ($E_c = 12.46\,\mathrm{keV}$) and kappa form electron injection spectrum, respectively. Right panel: the distribution of electrons for the energy $f_k(E)$ of the fitted kappa distribution (blue curve, total electron number density $n_k = 1.1 \times 10^9\,\mathrm{cm}^{-3}$, from Equation 8) and the ambient thermal plasma Maxwellian distribution (red curve, total electron number density $n_k = n_{th} = 2.4 \times 10^{10}\,\mathrm{cm}^{-3}$).

Parameters	vth+WTM(power-law)	vth+WTM(kappa)	
EM [10^{49} cm^{-3}]	0.0532	0.0532	Fixed
$k_B T$ [keV]	1.67	1.67	Fixed
n_{loop} [10^{10} cm^{-3}]	2.4	2.4	Fixed
$k_B T_{\text{loop}}$ [keV]	1.67	1.67	Fixed
L [Mm]	18.4	18.4	Fixed
$\dot{N}_0$ [10^{35} electrons sec^{-1}]	13.6 ± 1.3	20.5 ± 1.4	Free
δ	4.86 ± 0.05	N/A	Free
κ	N/A	8.85 ± 0.41	Free
E_c [keV]	12.46 ± 0.45	N/A	Free
$k_B T_\kappa$ [keV]	N/A	2.97 ± 0.17	Free
χ^2	0.91	1.06	N/A
Power [10^{28} erg/s]	3.66	2.95 for total; 1.51 above E_c	N/A

Table 2. The best-fit parameters and results of 2022 March 28 M4.0 flare using the warm-target model. The iso-thermal component and thermal properties of the warm-target model are fixed, and properties associated with the accelerated electrons are set free. The reduced χ^2 and nonthermal electron power P (for kappa-form electrons, the total power and power above power-law low energy cutoff E_c) are also listed.

tron distribution, same as 2011 February 24 flare, will decrease more rapidly at higher energy ($\kappa > \delta+1$). The nonthermal power generated by the injected electron spectrum (3.66 vs 2.95 $\times 10^{28}$ erg/s, for electrons in power-law and kappa form distribution, respectively) also exhibits significant dissimilarities. The kappa form electrons generate less nonthermal power $P_\kappa/P_{power-law} \approx 0.81$ despite larger total injection rates: 20.5 vs. 13.6 [10^{35} electrons sec^{-1}]. Figure 7 also illustrates a comparison between the distribution of accelerated kappa-form electrons (blue curve, total electron number density $n_k = 1.1 \times 10^9$ cm^{-3}) and ambient thermal Maxwellian distribution (red curve, total electron number density $n_{th} = 2.4 \times 10^{10}$ cm^{-3}, $k_B T = 1.67$ keV) in the right panel.

4. ANALYSIS TO THE FIT PARAMETERS AND FIT RESULTS

In this section, we will further investigate how well the three free kappa parameters ($\dot{N}_0$, κ, and T_κ) can be constrained by the fit with the warm-target model. We will provide the uncertainty of the fit parameters using different methods. Additionally, we will compare the total electron density n_k and average electron energy E_{avg} derived from the fit kappa-form spectrum with the corresponding thermal properties.

4.1. *2011 February 24 RHESSI flare*

In the previous section, we show that fitting using the functions *f_vth* and *f_thick_warm_kappa* involves three free parameters: $\dot{N}_0$, κ, and T_κ, all associated with the kappa distribution. To estimate the uncertainty of each parameter at different confidence levels, we apply the method used in Kontar et al. (2019). We began by assessing the uncertainty of total injection rate $\dot{N}_0$. We carry out spectral fits with $\dot{N}_0$ set at a fixed value while setting two other kappa parameters (κ, and T_κ) for free. By doing this, we can obtain the best-fit full χ^2 as well as the corresponding kappa index κ and kappa temperature T_κ at this fixed $\dot{N}_0$. Subsequently, we repeat these fits multiple times with different fixed $\dot{N}_0$ values and record the corresponding full χ^2 values. Further, we define $\Delta\chi^2 = \chi^2 - min(\chi^2)$, where $min(\chi^2)$ is the
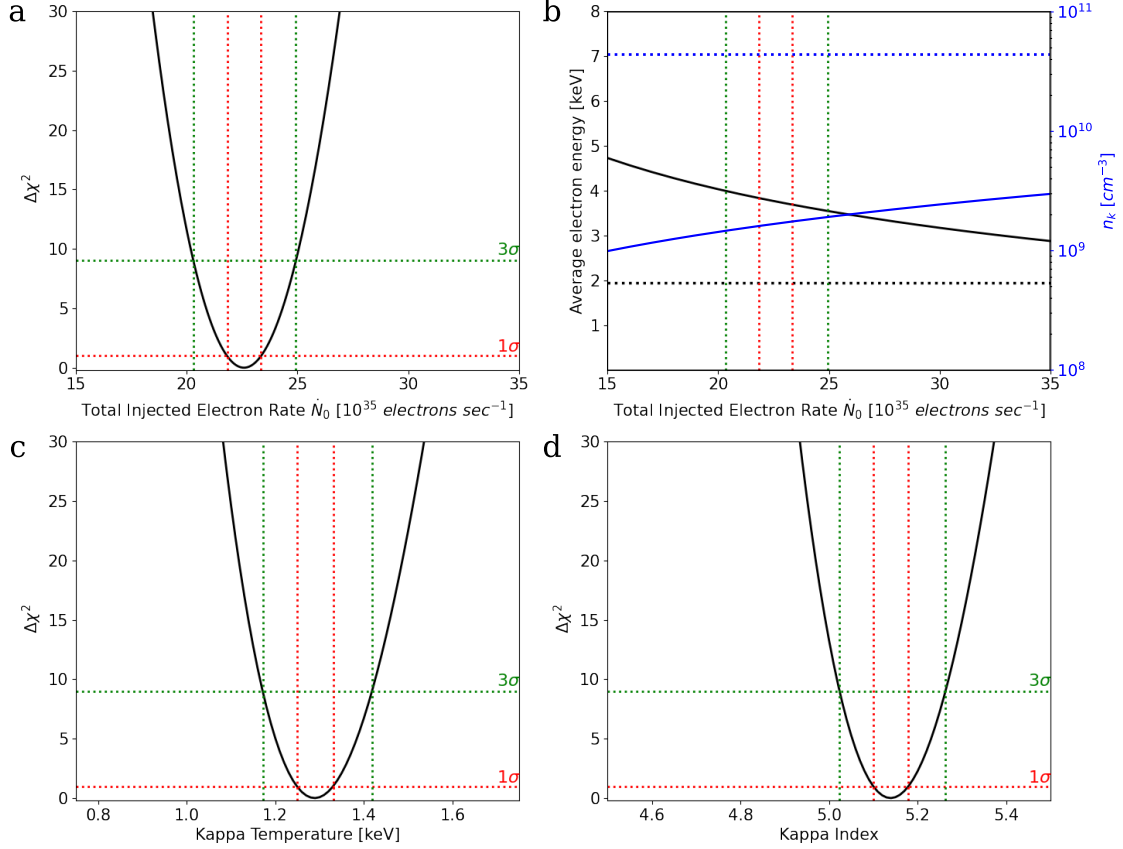
Figure 8. Panel a: $\Delta\chi^2$ against the given total injected electron rate ($\dot{N}_0$) fixed for the fit. The red and green horizontal lines represent the 1-σ and 3-σ uncertainty level, respectively. Red and green vertical lines correspond to the $\dot{N}_0$ range within the 1-σ and 3-σ uncertainty level, $22.5^{+0.8}_{-0.6} \times 10^{35}$ electrons sec^{-1}, and $22.5^{+2.4}_{-1.8}$ $\times 10^{35}$ electrons sec^{-1}, respectively. Panel b: Corresponding average electron energy E_{avg} (black curve) and number density n_k (blue curve) derived from the fit kappa-form electron spectrum with different fixed $\dot{N}_0$ in panel a. The red and green vertical lines represent the $\dot{N}_0$ range within the 1-σ and 3-σ uncertainty level, same as panel a. The black horizontal line represents the average electron energy from the thermal loop ($\frac{3}{2}k_B T_{\text{loop}}$) at 1.95 keV. The blue horizontal line represents the total number density of 4.4×10^{10} cm^{-3}, which is the number density of ambient coronal loop plasma and serve as a upper limit of the fit number density. We note that the fit results within the acceptable range satisfy the two constraints from average electron energy ($E_{avg-\kappa} > E_{avg-loop}$) and number density ($n_k < n_{\text{loop}}$). Panel c: same as panel a but the fixed parameter is kappa temperature $k_B T_\kappa$. The $k_B T_\kappa$ ranges within the 1-σ and 3-σ uncertainty level are $1.29^{+0.04}_{-0.04}$ keV and $1.29^{+0.13}_{-0.12}$ keV, respectively. Panel d: same as panel a but the fixed parameter is kappa index κ. The κ ranges within the 1-σ and 3-σ uncertainty level are $5.14^{+0.04}_{-0.04}$ and $5.14^{+0.12}_{-0.12}$, respectively.

minimum of all the obtained full χ^2 values. $\Delta\chi^2$ reaches 0 at the $\dot{N}_0$ value of 22.5×10^{35} electrons sec^{-1} (Figure 8 panel a), consistent with the best-fit results shown in Table 1. The $\Delta\chi^2$–$\dot{N}_0$ curve (Figure 8 panel a) displays a prominent minimum, and the $\Delta\chi^2$ value changes rapidly in the vicinity of this minimum. The $\dot{N}_0$ within the 1-σ uncertainty level (corresponding to a 68% confidence level, red horizontal dashed line in Figure 8 panel a) ranges $22.5^{+0.8}_{-0.6} \times 10^{35}$ electrons sec^{-1} (red vertical dashed lines in Figure
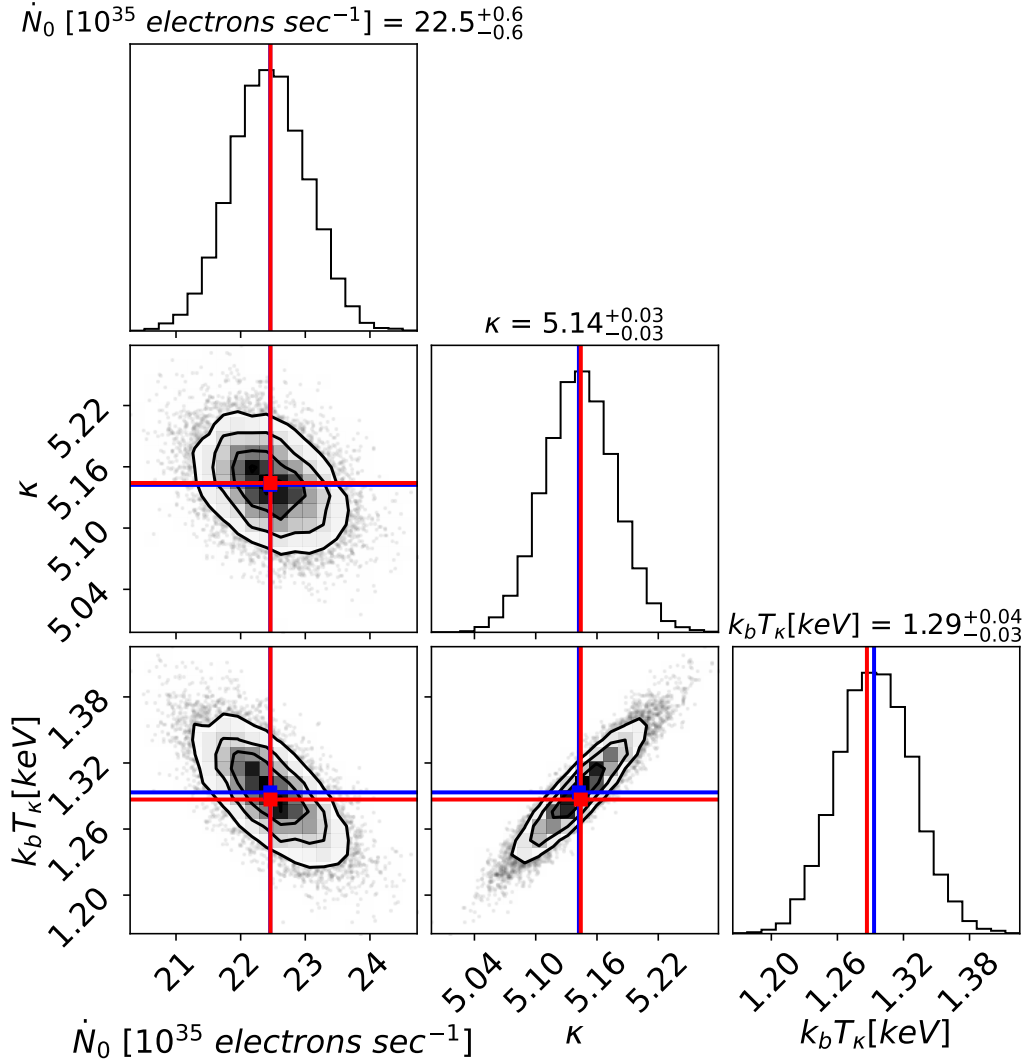
Figure 9. The coroner plot of the posterior probability function for the 2011 February 24 M3.5 flare obtained from the Monte Carlo analysis performed using `OSPEX`. The diagonal panels display the one-dimensional projected probability function for each parameter ($\dot{N}_0$, κ, and T_κ), and the remaining panels show the two-dimensional projection. The final fit results of the Monte Carlo analysis and the best-fit results of the forward fit are depicted in red and blue, respectively. Additionally, the plot includes the 1-σ level uncertainty range for each parameter: $\dot{N}_0 = 22.5^{+0.6}_{-0.6} \times 10^{35}$ electrons sec^{-1}, $\kappa = 5.14^{+0.03}_{-0.03}$, and $k_\mathrm{B}T_\kappa = 1.29^{+0.04}_{-0.03}$ keV.

8 panel a), and the $\dot{N}_0$ within the 3-σ uncertainty level (corresponding to a 99% confidence level, green horizontal dashed line in Figure 8 panel a) ranges $22.5^{+2.4}_{-1.8} \times 10^{35}$ electrons sec^{-1} (green vertical dashed lines in Figure 8 panel a). The $\Delta\chi^2$–$\dot{N}_0$ curve and the estimated uncertainty suggest that the $\dot{N}_0$ can be effectively constrained by the fit with the warm-target model.

The same approach is used to analyze two other kappa parameters, κ, and T_κ, for uncertainty. Both the $\Delta\chi^2$–T_κ (Figure 8 panel c) and $\Delta\chi^2$–κ (Figure 8 panel d) curves reveal a distinct minimum, similar to the $\Delta\chi^2$–$\dot{N}_0$ curve. The range of $k_\mathrm{B}T_\kappa$ for 1-σ and 3-σ uncertainty levels (red and green horizontal dashed lines in Figure 8 panel c) is $1.29^{+0.04}_{-0.04}$ keV and $1.29^{+0.13}_{-0.12}$ keV (red and green vertical dashed lines in Figure 8 panel c), respectively. The range of κ for 1-σ and 3-σ uncertainty levels (red and green
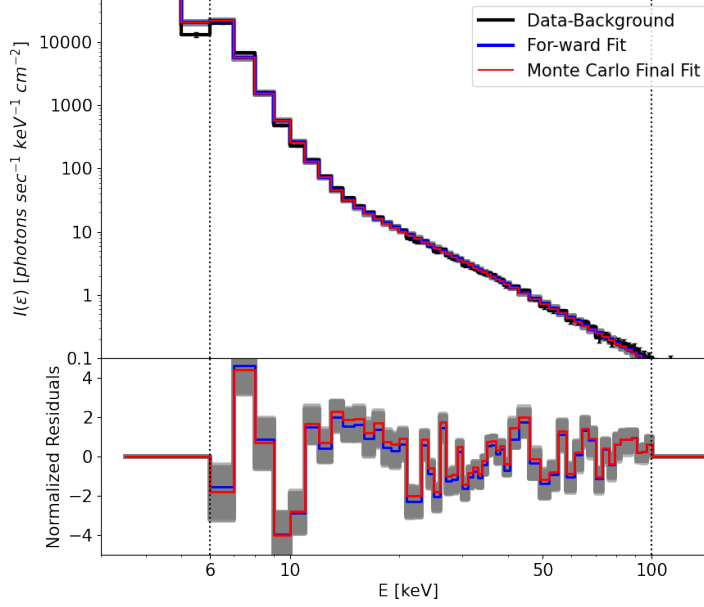
Figure 10. The upper panel depicts the photon spectrum of the observation (Background subtracted, black curve), the best-fit results obtained from the forward fit (blue curve), the final fit result generated by the Monte Carlo analysis (red curve), and the photon spectrum generated by the Monte Carlo sampling parameters (gray curves) of the 2011 February 24 M3.5 flare. The lower panel displays the normalized residuals associated with the corresponding fit spectrum.

horizontal dashed line in Figure 8 panel d) is $5.14^{+0.04}_{-0.04}$ and $5.14^{+0.12}_{-0.12}$ (red and green vertical dashed lines in Figure 8 panel d), respectively. The small fit uncertainties for all three kappa parameters indicate that all parameters can be accurately determined using the warm-target model.

In this study, we utilize the 3-σ uncertainty level to define the acceptable range of the fit parameters and investigate the physical properties within this acceptable range. One valuable property we examine is the average energy of the electrons E_{avg}. Here, we first adopt the acceptable range of $\dot{N}_0$, which falls between 20.3 and 24.9 $\times 10^{35}$ electrons sec^{-1}. Each given $\dot{N}_0$ within the acceptable range corresponds to a fit kappa-form electron spectrum. The average electron energy for the kappa-form electron spectrum E_{avg} is given by:

$$E_{avg} = \frac{\int_0^\infty E f_k(E)\, dE}{\int_0^\infty f_k(E)\, dE} = \frac{3}{2}\frac{\kappa}{\kappa - 2.5} k_B T_\kappa. \tag{15}$$

For comparison, the average electron energy of the Maxwellian electron spectrum is $E_{avg} = \frac{3}{2}k_B T$. The obtained E_{avg}–$\dot{N}_0$ curve is depicted by the black curve in Figure 8 panel b. It is worth noting that, within the acceptable range (green vertical dashed lines in Figure 8 panel b), the average electron energies derived from the kappa-form electron spectrum $E_{avg-\kappa}$ are consistently higher than the average electron energy of the thermal plasma in the target loop ($E_{avg-loop} = \frac{3}{2}k_B T_{loop}$ =1.95 keV, black horizontal dashed lines in Figure 8 panel b). According to Equation 8, the total electron number density n_k can be determined once the injection area A is known. We use the cross-area of the loop top X-ray coronal source ($A = \pi r^2 = 4.21 \times 10^{10}$ cm^2, red outlier contour in Figure 2 right panel) as the injection area A to calculate the total electron number density n_k. The n_k–$\dot{N}_0$ curve is shown in blue curve in Figure 8 panel b.

Within the acceptable range of $\dot{N}_0$, the total electron number density n_k is found to be lower than the thermal electron density of the target coronal loop n_{loop} (blue horizontal dashed lines in Figure 8 panel b, $4.4 \times 10^{10}\,\mathrm{cm}^{-3}$). While the electron injection area cannot be precisely determined, and it may be smaller than the observed loop cross area. n_k is unlikely to be higher than the loop density n_{loop}, which requires a extremely small injection area $A < 1.60 \times 10^9\,\mathrm{cm}^2$. The results indicate that the values of $E_{avg-\kappa}$ and n_k are physically reasonable when compared with the ambient thermal plasma. The fitted kappa-form electron spectrum and associated properties ($E_{avg-\kappa}$ and n_k) within the acceptable range for T_κ and κ closely resembles those obtained within the acceptable range for $\dot{N}_0$, and consistent with the previous findings. Consequently, we have opted not to display them in the plot.

In order to further evaluate how well the fit parameters can be determined and cross-check their uncertainty, we utilized the Monte Carlo analysis provided by OSPEX. Detailed information on this method is available in the 'Fit Parameter Uncertainty Analysis' section from Tolbert & Schwartz (2020). In addition, Ireland et al. (2013) discussed commonly used methods, including the Monte Carlo method, for estimating the constraint of fit parameters. The Monte Carlo analysis requires a predetermined best-fit result, which is available in Table 1. The Monte Carlo sampling explores the multidimensional parameter space ($\dot{N}_0$, κ, and T_κ) surrounding the best-fit results by assuming a Gaussian probability function for each parameter. Figure 9 shows the posterior probability density function for the three free parameters obtained from the Monte Carlo analysis. The final fit results of the Monte Carlo analysis, as well as the predetermined best-fit results from the forward fit, are also depicted in red and blue dots, respectively. The coroner plot diagonal panels show the one-dimensional projection of the probability density function. For the 2011 February 24 M3.5 flare, each parameter exhibits a prominent peak and a relatively narrow width, indicating that they are well-constrained around the best-fit results. The 1-σ uncertainty level range for each parameter is shown in Figure 9: $\dot{N}_0=22.5^{+0.6}_{-0.6} \times 10^{35}$ electrons sec^{-1}, $\kappa=5.14^{+0.03}_{-0.03}$, and $k_{\mathrm{B}}T_\kappa=1.29^{+0.04}_{-0.03}$ keV, comparable with the uncertainty obtained from the previous method. The non-diagonal panels display the probability density function projected for different parameter pairs, which illustrate the correlations between different parameters. We observed that κ and T_κ are positively correlated, while $\dot{N}_0$ is anti-correlated with κ and T_κ. The photon spectrum and normalized residuals generated by Monte Carlo sampling, Monte Carlo final fit result, and best forward fit result are shown in gray, red, and blue curves in Figure 10.

4.2. *2022 March 28 STIX flare*

We conducted the same analysis on the 2022 March 28 M4.0 flare observed by STIX. Similar to the 2011 February 24 M3.5 flare, the $\Delta\chi^2$–$\dot{N}_0$, $\Delta\chi^2$–T_κ, and $\Delta\chi^2$–κ curves (black curves in Figure 11 panel a, c, and d, respectively) all exhibit a prominent minimum. The ranges for each parameter at 1-σ and 3-σ uncertainty levels are listed below: for $\dot{N}_0$, $20.5^{+1.3}_{-1.2} \times 10^{35}$ electrons sec^{-1}, and $20.5^{+3.9}_{-3.8} \times 10^{35}$ electrons sec^{-1}; for $k_{\mathrm{B}}T_\kappa$, $2.97^{+0.17}_{-0.16}$ keV, and $2.97^{+0.55}_{-0.45}$ keV; for κ, $8.85^{+0.41}_{-0.38}$, and $8.85^{+1.45}_{-1.01}$. The spectral fit for the 2022 March 28 M4.0 flare, due to a narrow fit range (6–50 keV) and a 6% systematic error from STIX (2% for RHESSI), results in relatively larger uncertainties, particularly for T_κ and κ. However, these uncertainties still demonstrate that the warm target fit effectively constrains the fit parameters. We adopt the 3-σ uncertainty level as the acceptable range, consistent with our approach for the 2011 February 24 M3.5 flare. The derived average electron energy E_{avg} and total electron density n_k both satisfy $E_{avg-\kappa} > E_{avg-loop}$ and $n_k < n_{\mathrm{loop}}$ within the acceptable range (Figure 11 panel b). Additionally, the Monte Carlo analysis results are displayed in Figures 12 and 13. The 1-σ uncertainty level range for each parameter is: $\dot{N}_0=20.5^{+0.2}_{-0.2} \times 10^{35}$ electrons sec^{-1}, $\kappa=8.85^{+0.17}_{-0.14}$, and $k_{\mathrm{B}}T_\kappa=2.97^{+0.06}_{-0.05}$ keV. The
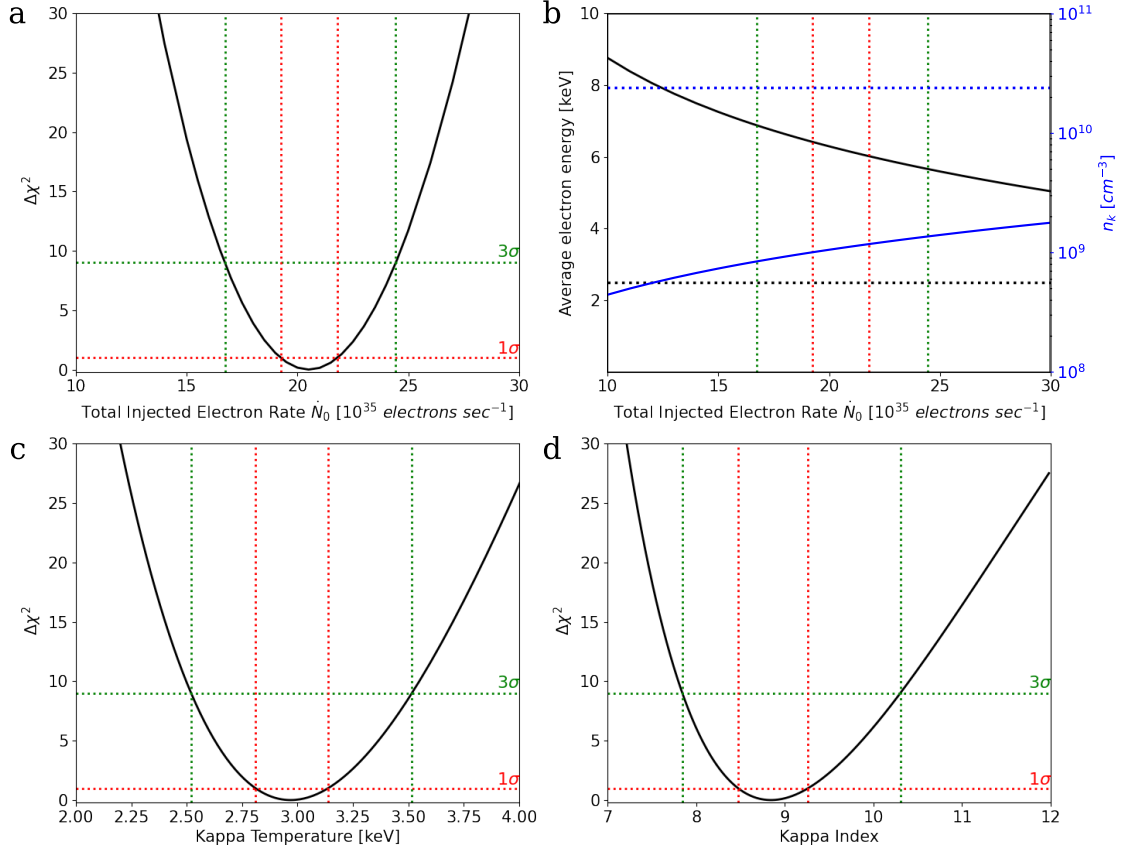
Figure 11. Same as Figure 8 but for 2022 March 28 M4.0 flare. Panel a: $\Delta\chi^2$ against the different total injected electron rate ($\dot{N}_0$). The red and green horizontal lines represent the 1-σ and 3-σ uncertainty level, respectively. Red and green vertical lines correspond to the $\dot{N}_0$ range within the 1-σ and 3-σ uncertainty level, $20.5^{+1.3}_{-1.2}$ $\times 10^{35}$ electrons sec^{-1}, and $20.5^{+3.9}_{-3.8}$ $\times 10^{35}$ electrons sec^{-1}, respectively. Panel b: Corresponding average electron energy E_{avg} (black curve) and number density n_k (blue curve) derived from the fit kappa-form electron spectrum in different fixed $\dot{N}_0$. The red and green vertical lines represent the $\dot{N}_0$ range within the 1-σ and 3-σ uncertainty level, same as panel a. The black horizontal line represents the average electron energy from the thermal loop ($\frac{3}{2}k_{\mathrm{B}}T_{\mathrm{loop}}$) at 2.51 keV. The blue horizontal line represents the electron number density of the ambient thermal plasma 2.4×10^{10} cm^{-3}. Panel c: same as panel a but the fixed parameter is kappa temperature. The $k_{\mathrm{B}}T_\kappa$ ranges within the 1-σ and 3-σ uncertainty level are $2.97^{+0.17}_{-0.16}$ keV and $2.97^{+0.55}_{-0.45}$ keV, respectively. Panel d: same as panel a but the fixed parameter is kappa index. The κ ranges within the 1-σ and 3-σ uncertainty level are $8.85^{+0.41}_{-0.38}$ and $8.85^{+1.45}_{-1.01}$, respectively.

correlations between these parameters are consistent with the findings from the 2011 February 24 M3.5 flare (Figure 12 diagonal panels).

5. SUMMARY

In this study, we utilized the warm-target model to analyze two GOES M-class limb flares. One M3.5 class flare occurred on February 24, 2011, and is observed by RHESSI, while STIX observed the other M4.0 class flare on March 28, 2022. We used the warm-target model due to its ability to accurately de-
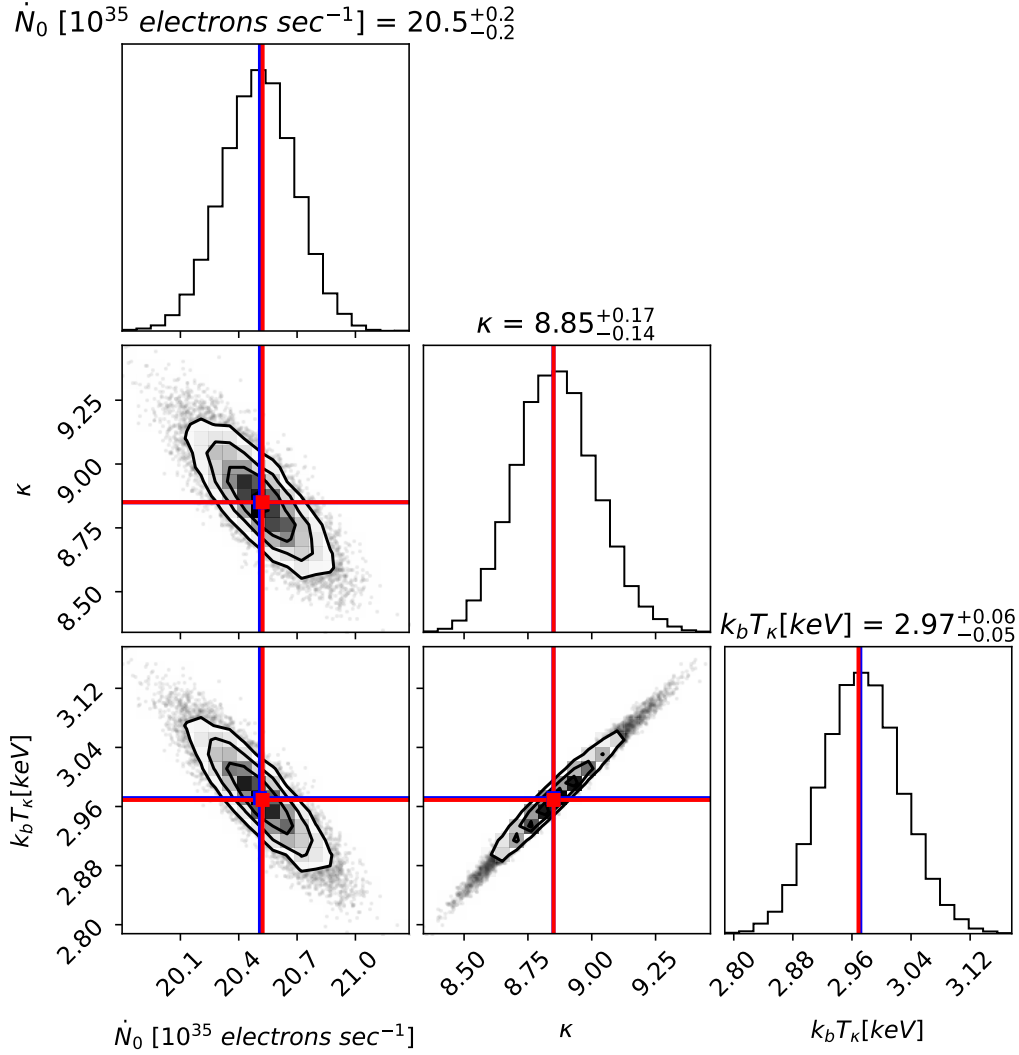
Figure 12. The coroner plot of the posterior probability function for the 2022 March 28 M4.0 flare obtained from the Monte Carlo analysis performed using OSPEX. Same as Figure 9, the diagonal panels display the one-dimensional projected probability function for each parameter ($\dot{N}_0$, κ, and T_κ), and the non-diagonal panels show the two-dimensional projection. The final fit results of the Monte Carlo analysis and the best-fit results of the forward fit are depicted in red and blue, respectively. The plot also includes the 1-σ level uncertainty range for each parameter: $\dot{N}_0=20.5^{+0.2}_{-0.2} \times 10^{35}$ electrons sec^{-1}, $\kappa=8.85^{+0.17}_{-0.14}$, and $k_BT_\kappa=2.97^{+0.06}_{-0.05}$ keV.

termine nonthermal electron properties, such as nonthermal power, which can hardly be constrained by the commonly used cold-target model. Unlike previous investigations, the kappa distribution is used to characterize the accelerated/injected electrons. Unlike the power-law distribution, the kappa distribution is finite as the electron speed approaches zero, thereby effectively covering the entire electron energy range without the requirement of an arbitrary low energy cutoff. Consequently, the fitted kappa-form electron spectrum can characterize electrons of which the kinetic energy falls below the X-ray instrument's sensitive range. The results of the fitting and subsequent analysis are summarized below:
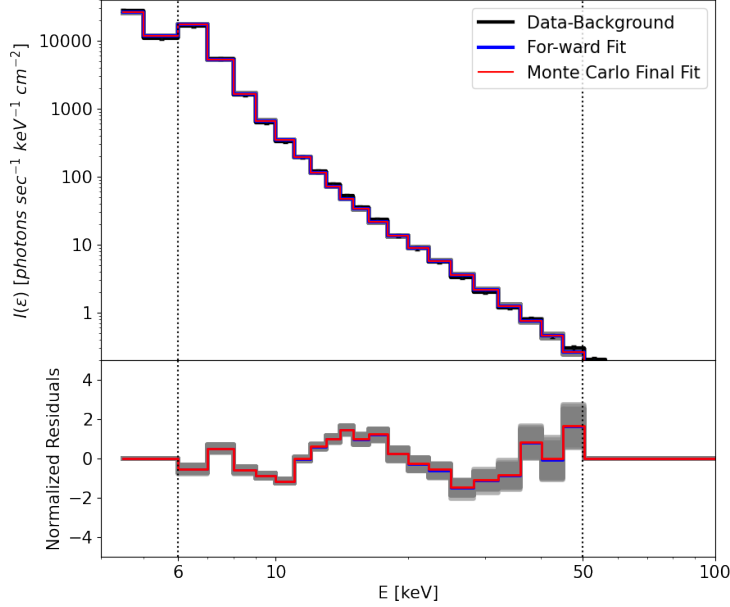
Figure 13. Same as Figure 10, but for 2022 March 28 M4.0 flare. The upper panel shows the photon spectrum of the observation (Background subtracted, black curve), the best-fit results obtained from the forward fit (blue curve), the final fit result generated by the Monte Carlo analysis (red curve), and the photon spectrum generated by the Monte Carlo sampling parameters (gray curves). The lower panel displays the normalized residuals associated with the corresponding fit spectrum.

- The best-fit results using the warm-target model in kappa-form injected electrons feature reasonable electron spectrum. For comparison, we also employed the warm-target model in the power-law electron distribution to fit the HXR spectrum. We found that the obtained power-law and kappa-form electron spectrum generate similar photon spectrum within the fitting range. However, the kappa-form electron spectrum produces less nonthermal power despite having a comparable or higher total injection rate $\dot{N}_0$. This energy difference is due to the behavior of the electron spectrum. The obtained kappa-form and power-law-form electron spectra exhibited similar behavior at the deka-keV level, while the kappa-form spectrum displayed a significantly lower flux below ~ 30 keV. Moreover, the kappa-form electron spectrum decreased more rapidly than the power-law spectrum ($\kappa > \delta + 1$) at higher energies (typically above 100 keV, out of the fit range).

- The fit with the warm-target model in kappa-form electron injection involves three free parameters ($\dot{N}_0$, κ, and T_κ). $\Delta\chi^2$-$\dot{N}_0$ curve reveals a prominent minimum, suggesting an accurate determination of $\dot{N}_0$ within a narrow range. For the M3.5 flare on February 24, 2011, $\dot{N}_0$ within 1-σ uncertainty level ranges $22.5^{+0.8}_{-0.6} \times 10^{35}$ electrons sec^{-1}, and the 3-σ uncertainty level range is $22.5^{+2.4}_{-1.8} \times 10^{35}$ electrons sec^{-1}. For the M4.0 flare on March 28, 2022, $\dot{N}_0$ within 1-σ uncertainty level ranges $20.5^{+1.3}_{-1.2} \times 10^{35}$ electrons sec^{-1}, and the 3-σ uncertainty level is $20.5^{+3.9}_{-3.8} \times 10^{35}$ electrons sec^{-1}. We apply the same analyses to the other two fit parameters, κ and T_κ, for their uncertainty. For the M3.5 flare on February 24, 2011, κ within 1-σ and 3-σ uncertainty level range is $5.14^{+0.04}_{-0.04}$ and $5.14^{+0.12}_{-0.12}$, respectively. $k_B T_\kappa$ within 1-σ and 3-σ uncertainty level range is $1.29^{+0.04}_{-0.04}$ keV and $1.29^{+0.13}_{-0.12}$ keV, respectively. For the M4.0 flare on March 28, 2022, κ within 1-σ and 3-σ uncertainty

level range is $8.85^{+0.41}_{-0.38}$ and $8.85^{+1.45}_{-1.01}$, respectively. $k_B T_\kappa$ within 1-σ and 3-σ uncertainty level range is $2.97^{+0.17}_{-0.16}$ keV and $2.97^{+0.55}_{-0.45}$ keV, respectively. All the three parameters, $\dot{N}_0$, T_κ and κ are tightly constrained within a narrow range. Additionally, we carry out a Monte Carlo analysis to further confirm the effectiveness in determining the fit parameters with the warm-target model. The resulting posterior probability density function for all three kappa parameters demonstrates distinct peaks and relatively narrow widths, indicating well-constrained fit parameters. The Monte Carlo analysis also provide a 1-σ level uncertainty for each parameter: for 2011 February 24 M3.5 flare, $\dot{N}_0 = 22.5^{+0.6}_{-0.6} \times 10^{35}$ electrons sec^{-1}, $\kappa = 5.14^{+0.03}_{-0.03}$, and $k_B T_\kappa = 1.29^{+0.04}_{-0.03}$ keV; for 2022 March 28 M4.0 flare, $\dot{N}_0 = 20.5^{+0.2}_{-0.2} \times 10^{35}$ electrons sec^{-1}, $\kappa = 8.85^{+0.17}_{-0.14}$, and $k_B T_\kappa = 2.97^{+0.06}_{-0.05}$ keV.

- Unlike the power-law distribution, which requires a low energy cut-off E_c, the kappa-form electron spectrum works for all energies, anchored at zero speed, and extend to the speed of light. Therefore, the kappa distribution facilitates the determination of the accelerated electron number density n_k (with the information of the injection area A) and the average electron energy E_{avg}. For both flares in this study, we find that, the derived total electron energy density is lower than the thermal number density of the target loop ($n_k < n_{loop}$, 1.7×10^9 cm^{-3} $< 4.4 \times 10^{10}$ cm^{-3} and 1.1×10^9 cm^{-3} $< 2.4 \times 10^{10}$ cm^{-3} for 2011 February 24 and 2022 March 28 flare, respectively), while the average electron energy surpasses that of the ambient Maxwellian thermal plasma ($E_{avg-\kappa} > E_{avg-loop}$, 3.77 keV > 1.95 keV and 6.21 keV > 2.51 keV for 2011 February 24 and 2022 March 28 flare, respectively).

In this study, we have demonstrated that the fit with the warm-target model provides a convincing kappa-form accelerated electron spectrum. The associated kappa distribution parameters are valuable for understanding electron acceleration and transport. Here, we follow the model proposed by Bian et al. (2014), which uses the Fokker-Planck equation to analyze the evolution of flare-associated electrons. Bian et al. 2014 proposed that the kappa distribution arises from stochastic acceleration in the presence of Coulomb collisions and velocity diffusion. The kappa index κ is given by $\kappa = \frac{\tau_{acc}(v)}{2\tau_c(v)}$. The collisional deceleration time can be estimated as: $\tau_c(v) \approx v^3/\Gamma$, where the collisional parameter $\Gamma = 2Kn/m_e^2$. Here, we take the parameters from the 2011 February 24 M3.5 flare event for study. For the upper limit of electron energy E_l enabling the complete stop within the target, we have $E_l = \sqrt{2KnL} \approx 19.0$ keV. At E_l, we have the electron speed $v_l = 8.0 \times 10^9$ cm/s and the collisional deceleration time $\tau_c(v_l) \approx 0.71$ seconds. Thus the acceleration time can be determined by $\tau_{acc}(v_l) = 2\kappa\tau_c(v_l) \approx 7.33$ seconds. The collisional diffusion time $\tau_d(v_l) = \frac{2v_l^5}{\Gamma v_{te}^2} \approx 19.77$ seconds, where thermal speed $v_{te} = \sqrt{2k_B T_\kappa}/m_e \approx 2.1 \times 10^9$ cm/s.

The ratio between the density of accelerated nonthermal electrons (n_{nth}) and ambient thermal electrons (n_{th}) can provide valuable insights into electron acceleration during solar flares. Previous studies have shown that the ratio of nonthermal electrons to protons ($n_p = n_{nth} + n_{th}$ in the hydrogen plasma) is on the order of approximately 1% (Oka et al. 2013). In this study, we determined the density of accelerated nonthermal electrons in corona by integrating the kappa electron spectrum over 10 keV($n_{nth}[> 10$ keV$] \sim 1.2 \times 10^8$ cm^{-3}, and 2.0×10^8 cm^{-3} for 2011 February 24 M3.5 and 2022 March 28 M4.0 flare, respectively). For the thermal electron density in the flare site, We take the loop electron density obtained from the X-ray thermal component ($n_{th} = n_{loop}$). The ratio between the density of coronal accelerated nonthermal electrons and ambient protons is found to be less than 1% ($n_{nth}/n_p \sim 0.003$,

and 0.008, for 2011 February 24 M3.5 and 2022 March 28 flare, respectively), consistent with recent studies (Kontar et al. 2023).

Here, we note the electron number density is calculated using Equation 8 and is dependent on the injection area A. We estimated the injection area A using 50% of the loop top X-ray source contour. The resulting total injected electron density is approximately an order of magnitude lower than the estimated coronal loop thermal electron density ($1.7 \times 10^9 \, \mathrm{cm}^{-3} < 4.4 \times 10^{10} \, \mathrm{cm}^{-3}$ and $1.1 \times 10^9 \, \mathrm{cm}^{-3} < 2.4 \times 10^{10} \, \mathrm{cm}^{-3}$ for 2011 February 24 and 2022 March 28 flare, respectively). It is important to note that the electron injection in the coronal region may be non-uniform in height. According to Jeffrey et al. (2015), the actual injection might be smaller. In this study, we are utilizing the spatially integrated spectrum for analysis. At present, the signal-to-noise ratio does not sufficiently support precise spatially resolved spectral diagnostics at the arcsecond scale. Once we obtain the spatially resolved spectral information from the improved X-ray observations, the electron density derived from the kappa distribution will be more persuasive.

Since both the RHESSI and Sol-O/STIX are not sensitive to photons below ∼3-6 keV, the thermal properties obtained from RHESSI X-ray spectral diagnostics could differ from those obtained from SDO/AIA EUV diagnostics (Battaglia & Kontar 2013). Furthermore, thermal properties inferred from the observed X-ray spectrum are likely to be height dependent (Jeffrey et al. 2015). The obtained kappa-form energetic electrons allows for a more comprehensive combined study of the X-ray and EUV diagnostics. Potential future applications of the derived kappa distribution also include studying acceleration mechanisms based on the average electron energy and nonthermal power.

REFERENCES

Alaoui, M., & Holman, G. D. 2017, ApJ, 851, 78, doi: 10.3847/1538-4357/aa98de

Arnold, H., Drake, J. F., Swisdak, M., et al. 2021, PhRvL, 126, 135101, doi: 10.1103/PhysRevLett.126.135101

Aschwanden, M. J., Holman, G., O'Flannagain, A., et al. 2016, ApJ, 832, 27, doi: 10.3847/0004-637X/832/1/27

Aschwanden, M. J., Kontar, E. P., & Jeffrey, N. L. S. 2019, ApJ, 881, 1, doi: 10.3847/1538-4357/ab2cd4

Aschwanden, M. J., Caspi, A., Cohen, C. M. S., et al. 2017, ApJ, 836, 17, doi: 10.3847/1538-4357/836/1/17

Battaglia, M., & Benz, A. O. 2006, A&A, 456, 751, doi: 10.1051/0004-6361:20065233

Battaglia, M., & Kontar, E. P. 2011, A&A, 533, L2, doi: 10.1051/0004-6361/201117605

—. 2012, ApJ, 760, 142, doi: 10.1088/0004-637X/760/2/142

—. 2013, ApJ, 779, 107, doi: 10.1088/0004-637X/779/2/107

Battaglia, M., Motorina, G., & Kontar, E. P. 2015, ApJ, 815, 73, doi: 10.1088/0004-637X/815/1/73

Benz, A. O. 2017, Living Reviews in Solar Physics, 14, 2, doi: 10.1007/s41116-016-0004-3

Bian, N. H., Emslie, A. G., Stackhouse, D. J., & Kontar, E. P. 2014, ApJ, 796, 142, doi: 10.1088/0004-637X/796/2/142

Brown, J. C. 1971, SoPh, 18, 489, doi: 10.1007/BF00149070

Brown, J. C., Emslie, A. G., Holman, G. D., et al. 2006, ApJ, 643, 523, doi: 10.1086/501497

Brown, J. C., Emslie, A. G., & Kontar, E. P. 2003, ApJL, 595, L115, doi: 10.1086/378169

Cheung, M. C. M., Boerner, P., Schrijver, C. J., et al. 2015, ApJ, 807, 143, doi: 10.1088/0004-637X/807/2/143

Collier, M. R., Hamilton, D. C., Gloeckler, G., Bochsler, P., & Sheldon, R. B. 1996, Geophys. Res. Lett., 23, 1191, doi: 10.1029/96GL00621

Craig, I. J. D., & Brown, J. C. 1976, A&A, 49, 239

Drummond, W. E., & Pines, D. 1964, Annals of
Physics, 28, 478,
doi: 10.1016/0003-4916(64)90205-2

Effenberger, F., Rubio da Costa, F., Oka, M., et al.
2017, ApJ, 835, 124,
doi: 10.3847/1538-4357/835/2/124

Emslie, A. G. 1980, ApJ, 235, 1055,
doi: 10.1086/157709

Emslie, A. G., Kontar, E. P., Krucker, S., & Lin, R. P.
2003, ApJL, 595, L107, doi: 10.1086/378931

Emslie, A. G., & Smith, D. F. 1984, ApJ, 279, 882,
doi: 10.1086/161959

Galloway, R. K., MacKinnon, A. L., Kontar, E. P., &
Helander, P. 2005, A&A, 438, 1107,
doi: 10.1051/0004-6361:20042137

Hannah, I. G., & Kontar, E. P. 2012, A&A, 539, A146,
doi: 10.1051/0004-6361/201117576

Hannah, I. G., Kontar, E. P., & Sirenko, O. K. 2009,
ApJL, 707, L45,
doi: 10.1088/0004-637X/707/1/L45

Haug, E. 1998, SoPh, 178, 341,
doi: 10.1023/A:1005098624121

Högbom, J. A. 1974, A&AS, 15, 417

Holman, G. D. 2012, ApJ, 745, 52,
doi: 10.1088/0004-637X/745/1/52

Holman, G. D., & Benka, S. G. 1992, ApJL, 400, L79,
doi: 10.1086/186654

Holman, G. D., Aschwanden, M. J., Aurass, H., et al.
2011, SSRv, 159, 107,
doi: 10.1007/s11214-010-9680-9

Imada, S., Hirai, M., Hoshino, M., & Mukai, T. 2011,
Journal of Geophysical Research (Space Physics),
116, A08217, doi: 10.1029/2011JA016576

Inglis, A. R., & Christe, S. 2014, ApJ, 789, 116,
doi: 10.1088/0004-637X/789/2/116

Ireland, J., Tolbert, A. K., Schwartz, R. A., Holman,
G. D., & Dennis, B. R. 2013, ApJ, 769, 89,
doi: 10.1088/0004-637X/769/2/89

Jeffrey, N. L. S., Kontar, E. P., Bian, N. H., & Emslie,
A. G. 2014, ApJ, 787, 86,
doi: 10.1088/0004-637X/787/1/86

Jeffrey, N. L. S., Kontar, E. P., & Dennis, B. R. 2015,
A&A, 584, A89,
doi: 10.1051/0004-6361/201526665

Jeffrey, N. L. S., Krucker, S., Stores, M., et al. 2024,
ApJ, 964, 145, doi: 10.3847/1538-4357/ad236f

Kašparová, J., & Karlický, M. 2009, A&A, 497, L13,
doi: 10.1051/0004-6361/200911898

Knight, J. W., & Sturrock, P. A. 1977, ApJ, 218, 306,
doi: 10.1086/155683

Kontar, E. P., Emslie, A. G., Motorina, G. G., &
Dennis, B. R. 2023, ApJL, 947, L13,
doi: 10.3847/2041-8213/acc9b7

Kontar, E. P., Hannah, I. G., & MacKinnon, A. L.
2008, A&A, 489, L57,
doi: 10.1051/0004-6361:200810719

Kontar, E. P., Jeffrey, N. L. S., & Emslie, A. G. 2019,
ApJ, 871, 225, doi: 10.3847/1538-4357/aafad3

Kontar, E. P., Jeffrey, N. L. S., Emslie, A. G., & Bian,
N. H. 2015, ApJ, 809, 35,
doi: 10.1088/0004-637X/809/1/35

Kontar, E. P., Brown, J. C., Emslie, A. G., et al. 2011,
SSRv, 159, 301, doi: 10.1007/s11214-011-9804-x

Krall, N. A., & Trivelpiece, A. W. 1973, Principles of
plasma physics (Tokyo: McGraw-Hill Kogakusha)

Krucker, S., Hurford, G. J., Grimm, O., et al. 2020,
A&A, 642, A15,
doi: 10.1051/0004-6361/201937362

Landi, E., Young, P. R., Dere, K. P., Del Zanna, G., &
Mason, H. E. 2013, ApJ, 763, 86,
doi: 10.1088/0004-637X/763/2/86

Lin, R. P., & Hudson, H. S. 1976, SoPh, 50, 153,
doi: 10.1007/BF00206199

Lin, R. P., Dennis, B. R., Hurford, G. J., et al. 2002,
SoPh, 210, 3, doi: 10.1023/A:1022428818870

Ma, C.-y., & Summers, D. 1998, Geophys. Res. Lett.,
25, 4099, doi: 10.1029/1998GL900108

Mace, R. L., & Hellberg, M. A. 1995, Physics of
Plasmas, 2, 2098, doi: 10.1063/1.871296

Maksimovic, M., Zouganelis, I., Chaufray, J. Y., et al.
2005, Journal of Geophysical Research (Space
Physics), 110, A09104, doi: 10.1029/2005JA011119

Müller, D., St. Cyr, O. C., Zouganelis, I., et al. 2020,
A&A, 642, A1, doi: 10.1051/0004-6361/202038467

Oka, M., Ishikawa, S., Saint-Hilaire, P., Krucker, S.,
& Lin, R. P. 2013, ApJ, 764, 6,
doi: 10.1088/0004-637X/764/1/6

Oka, M., Krucker, S., Hudson, H. S., & Saint-Hilaire,
P. 2015, ApJ, 799, 129,
doi: 10.1088/0004-637X/799/2/129

Purkhart, S., Veronig, A. M., Dickson, E. C. M., et al.
2023, A&A, 679, A99,
doi: 10.1051/0004-6361/202346354

Rhee, T., Ryu, C.-M., & Yoon, P. H. 2006, Journal of
Geophysical Research (Space Physics), 111,
A09107, doi: 10.1029/2006JA011682

Rochus, P., Auchère, F., Berghmans, D., et al. 2020,
A&A, 642, A8, doi: 10.1051/0004-6361/201936663

Ryu, C. M., Rhee, T., Umeda, T., Yoon, P. H., & Omura, Y. 2007, Physics of Plasmas, 14, 100701, doi: 10.1063/1.2779282

Schwartz, R. A., Csillaghy, A., Tolbert, A. K., et al. 2002, SoPh, 210, 165, doi: 10.1023/A:1022444531435

Shao, C., & Huang, G. 2009, ApJ, 691, 299, doi: 10.1088/0004-637X/691/1/299

Spitzer, L. 1962, Physics of Fully Ionized Gases

Stackhouse, D. J., & Kontar, E. P. 2018, A&A, 612, A64, doi: 10.1051/0004-6361/201730708

Sui, L., Holman, G. D., Dennis, B. R., et al. 2002, SoPh, 210, 245, doi: 10.1023/A:1022417832283

Syrovatskii, S. I., & Shmeleva, O. P. 1972, Soviet Ast., 16, 273

Tolbert, K., & Schwartz, R. 2020, OSPEX: Object Spectral Executive, Astrophysics Source Code Library, record ascl:2007.018. https://ascl.net/2007.018

Vandas, M. 1989, Bulletin of the Astronomical Institutes of Czechoslovakia, 40, 175

Vedenov, A. A., & Velikhov, E. P. 1963, Soviet Journal of Experimental and Theoretical Physics, 16, 682

Vocks, C., & Mann, G. 2003, ApJ, 593, 1134, doi: 10.1086/376682

Yoon, P. H., Rhee, T., & Ryu, C.-M. 2006, Journal of Geophysical Research (Space Physics), 111, A09106, doi: 10.1029/2006JA011681

Zharkova, V. V., & Gordovskyy, M. 2006, ApJ, 651, 553, doi: 10.1086/506423